Eur. Phys. J. C (2026) 86:15
https://doi.org/10.1140/epjc/s10052-025-15196-5

THE EUROPEAN PHYSICAL JOURNAL C

Regular Article - Theoretical Physics

Quantum gravitational corrections at third-order curvature, acoustic analog black holes and their quasinormal modes

R. Casadio[1,2,a], **C. Noberto Souza**[3,b], **R. da Rocha**[4,c]

[1] Dipartimento di Fisica e Astronomia, Università di Bologna, Via Irnerio 46, 40126 Bologna, Italy
[2] I.N.F.N., Sezione di Bologna, I.S. FLAG, Viale B. Pichat 6/2, 40127 Bologna, Italy
[3] Center for Natural and Human Sciences, Federal University of ABC, 09210-580 Santo André, Brazil
[4] Center of Mathematics, Federal University of ABC, 09210-580 Santo André, Brazil

Received: 20 July 2025 / Accepted: 10 December 2025

Abstract Quasinormal modes for bosonic (scalar, electromagnetic, and axial gravitational) and fermionic field perturbations, radiated from black holes that carry quantum gravitational corrections at third order in the curvature to the Schwarzschild solution, are scrutinized from the propagation of analog transonic sound waves across a de Laval nozzle. The thermodynamic variables, the nozzle geometry, the Mach number, and the thrust coefficient are computed as functions of the parameter driving the effective action for quantum gravity containing a dimension-six local operator beyond general relativity. The quasinormal modes for quantum gravitational corrected analog black holes are also determined for higher overtones, yielding a more precise description of the quantum-corrected ringdown process and the gravitational waveform way before the fundamental mode sets in.

1 Introduction

Black holes (BHs) are expected to emit quantum radiation, which makes them remarkable tools for exploring the connection between quantum mechanics, thermodynamics, and gravity. The interplay among these theoretical aspects is encompassed by the Bekenstein–Hawking entropy. In particular, the entropy of a Schwarzschild BH can be accounted for by using effective field theoretical methods to calculate quantum gravitational corrections to the Bekenstein–Hawking entropy, which induce quantum corrections to the black body factors of Schwarzschild BHs [1,2].

Quantum gravity corrections are expected to emerge in gravitational backgrounds beyond the Einstein–Hilbert action of General Relativity (GR). Invariance under diffeomorphism is a fundamental symmetry of gravity, and the Einstein–Hilbert action can therefore be viewed as the deep-infrared and lowest-energy approximation of a more complete action involving higher-order curvature operators that induce quantum corrections. The sum of operators constituting the effective action for quantum gravity has to be truncated somehow, for the task of viably deriving the equations of motion that correspond to physically sound solutions [3–8]. Higher-order curvature operators are commonly used in effective approaches to quantum gravity. Relevant phenomenological aspects of quantum gravity, quantum gravitational corrected BHs, and some of their physical signatures were addressed in Refs. [9–18] also encompassing effective field theories (EFTs) [19–23]. Quantum gravity corrections were explored in the context of hydrodynamics in Refs. [24–26], with several applications.

Corrections to the Einstein–Hilbert gravity at 1-loop were computed by 't Hooft and Veltman [27], whereas Goroff and Sagnotti addressed quantum gravitational corrections at third-order in curvature as 2-loop quantum gravitational corrections to gravity [28]. In this context, Refs. [29–32] studied Einstein cubic gravity and effective theories of gravity, while quantum gravity with a third-order curvature term was studied in Refs. [33–37]. The effect of third-order curvature corrections to gravity and the consequence for thermal and hydrodynamical properties of a dual gauge theory describing quantum-corrected transport coefficients of the quark-gluon plasma were analyzed in Ref. [38].

One can explore bosonic and fermionic perturbations of BHs with quantum corrections for the Schwarzschild metric, as analytical solutions to the equations of motion associated

[a] e-mail: casadio@bo.infn.it
[b] e-mail: christian.noberto@ufabc.edu.br
[c] e-mail: roldao.rocha@ufabc.edu.br (corresponding author)

Published online: 08 January 2026

with a more general action involving higher-order curvature operators. Quasinormal (QN) modes are a fundamental feature of the gravitational signal emitted by compact objects in several astrophysical processes. Their eigenfrequencies manifest relevant information about the nature of the emitting source and its inner structure as well. The BH stability under perturbations is intricately associated with the inner features of the BH itself. Typically, the BH stability can be investigated by examining the evolution of field perturbations on the BH background or during BH mergers. The end state of astrophysical binary BH mergers is a perturbed single BH, characterized by the final remnant mass and angular momentum. When a BH is perturbed, it can emit gravitational waves (GWs), primarily characterized by QN modes. The term quasinormal contrasts with the usual normal modes in Newtonian gravity, since they damp after emitting GWs [39–42].

Collisions between BHs go through three stages: the inspiral, the merger, and the ringdown phases. With the LIGO/Virgo unprecedented discovery of GWs from merging BHs [43,44], the ringdown phase was detected in the GW signal, consisting of fast decaying oscillations characterised by eigenfrequencies over characteristic timescales. The QN spectra of more regular compact objects differ drastically from those that originate from perturbed BHs, although they still exhibit a comparable ringdown phase [45]. QN modes could also appear as echoes [46–51]. Several studies have robustly established that the QN frequencies of a BH are solely determined by the characteristics of the BH itself and the fields present in the perturbation process [52–55]. QN modes of spherically symmetric sources can be split into spin-weighted spherical harmonics of order ℓ and degree m. For each pair (ℓ, m), there exists a discrete set of complex frequencies denoted $\omega_{\ell mn}$, where n indexes the overtone. The oscillatory behaviour is described by the real part of $\omega_{\ell mn}$, whereas the imaginary part is related to the damping timescale, or equivalently, the inverse of the decay rate. The overtone index orders the QN modes for decreasing damping timescales so that the fundamental mode $n = 0$ corresponds to the least-damped mode and is the longest-lived [42].

The main goal of this work is to study BHs that carry quantum gravitational corrections at third order in the curvature expansion through the QN modes of analog models. Beyond providing insights into the stability of the BH spacetime, QN frequencies are crucial for determining the parameters that characterise these quantum-corrected BHs. Acoustic waves travelling through inviscid and inhomogeneous fluid flows have been shown to emulate waves on BH backgrounds. In any transonic fluid flow, while sound waves can move from subsonic to supersonic regions, they are prevented from propagating in the opposite direction. Thus, the critical sonic point, where the sound velocity matches the fluid velocity, behaves as an acoustic horizon, similar to an event horizon for sound waves. For a fluid flow in a nozzle, this horizon may emerge at the nozzle throat, which is the narrowest part of the tube [56]. Numerous analog gravity models have been formulated, and a wide range of experiments have been conducted and designed to observe the analog of QN ringing. Apart from the importance of experimental validation, analog gravity models are essential in theoretical contexts to enhance our comprehension of BH physics. Refs. [57–59] indicated that the QN ringing in sound waves is generated by acoustic BHs, analogous to the way BHs emit QN ringing in GWs. It offers the potential to observe BH QN ringing in laboratory conditions involving de Laval nozzles [60–63]. Since some gravitational excitations in BH scenarios can be described similarly to QN modes of sound waves in a nozzle, one can indirectly investigate quantum gravity corrections to BHs within the context of aerodynamics.

In this work, we analyse QN modes of BHs that incorporate quantum gravitational corrections at third order in the curvature expansion through transonic waves in a de Laval nozzle. We will show how BHs carrying quantum gravitational corrections can be mapped into analog gravity models, to test some of their features in a laboratory. Given the absence of observational support for quantum corrections to BHs, such experiments in aerodynamics can improve our understanding of the physical signatures of quantum gravity. The closer a BH mass is to the Planck mass, the larger the quantum gravitational corrections are expected to set in. We also investigate a large range of BH masses, from the Planck scale to stellar and astrophysical scales, showing that quantum gravitational corrections to the nozzle geometry, thermodynamic variables, Mach number, and thrust coefficients are more significant for smaller masses. This could be relevant for primordial BHs and their analogues. Sect. 2 aims to present quantum gravitational corrections in third order in the curvature expansion concerning BHs. In Sect. 3, we explore the relationship between perturbations on BH geometries and sound waves within a de Laval nozzle, outlining the conditions and constraint equations under which the analogy holds. Spinor, scalar, vector, and tensor perturbations of fluid flows in analog aerodynamics are proposed to probe quantum gravity-corrected BHs experimentally. Sect. 4 demonstrates how the parameters affecting quantum gravitational corrections at third order in the curvature expansion concerning BH parameters correspond to the nozzle geometry, thermodynamic variables, Mach number, and thrust coefficient. For it, the QN mode frequencies are calculated using the Mashhoon method, followed by a computation of the quality factor for the analog de Laval nozzle. Higher overtones are also computed and discussed, yielding a precise description of the GW form way before the fundamental mode dominates. The ringdown of the quantum gravitational-corrected BH is therefore addressed, improving the extraction of information from quantum gravity-corrected BH sources. Finally,

Sect. 5 reviews the primary findings and presents concluding remarks. Appendix A analyzes the de Laval nozzle geometry, thermodynamic variables, Mach number, and thrust coefficient for fixed representative values of the quantum gravitational correction parameter and BH masses typically varying in the range from the Planck mass to astrophysical BHs.

2 Quantum gravitational corrections at third-order curvature

Quantum gravitational corrections to the entropy of Schwarzschild BHs can be obtained using effective field theoretical methods to calculate the Bekenstein–Hawking entropy [1,2]. Starting from the Wald entropy formula

$$S_{\rm WALD} = -2\pi \lim_{r\to r_{\rm H}} \int {\rm d}\sigma\, \epsilon_{\mu\nu}\epsilon_{\rho\sigma} \frac{\partial \mathcal{L}}{\partial R_{\mu\nu\rho\sigma}} \tag{1}$$

where $\mathrm{d}\sigma = r^2 \sin\theta\, d\theta\, d\varphi$ is the area element on spheres, $\mathcal{L}$ is the Lagrangian of the model, $R_{\mu\nu\rho\sigma}$ denotes the Riemann tensor, and $r_{\rm H} = 2G_{\rm N}M$ is the horizon radius. Quantum corrections in the metric modify the position of the event horizon and, hence, Eq. (1). The effective action of quantum gravity, at second order in the curvature, with cosmological constant set to zero, has a local sector [64–66]

$$S_{\rm EFT} = \int \sqrt{|g|}{\rm d}^4x \left[\frac{R}{16\pi G_{\rm N}} + c_1(\mu)R^2 + c_2(\mu)R_{\mu\nu}R^{\mu\nu} + c_3(\mu)R_{\mu\nu\rho\sigma}R^{\mu\nu\rho\sigma} + \mathcal{L}_{\rm M}\right], \tag{2}$$

where μ denotes the renormalization scale, and $\mathcal{L}_{\rm M}$ is the matter Lagrangian, whereas the nonlocal sector is given by

$$\Gamma^{(2)}_{\rm NL} = \int \sqrt{|g|}{\rm d}^4x \left[\alpha R \log\left(\frac{\Box}{\mu^2}\right) R + \beta R_{\mu\nu} \log\left(\frac{\Box}{\mu^2}\right) R^{\mu\nu} + \gamma R_{\mu\nu\rho\sigma} \log\left(\frac{\Box}{\mu^2}\right) R^{\mu\nu\rho\sigma} + \mathcal{O}(M_{\rm PL}^{-2})\right], \tag{3}$$

where $M_{\rm PL}$ is the reduced Planck mass and $c_i(\mu)$, α, β, γ denote the Wilson coefficients. Ref. [1] showed the absence of quantum corrections to the Schwarzschild metric, up to second order in curvature [67,68]. It implies that the horizon radius remains unchanged and the quantum-corrected Wald entropy can be computed at second order, by Eqs. (2) and (3), as [1]

$$S^{(2)}_{\rm WALD} = \frac{A}{4G_{\rm N}} + 64\pi^2 \left\{c_3(\mu) + \gamma\left[\log\left(4G_{\rm N}^2M^2\mu^2\right) - 2 + 2\gamma_{\rm E}\right]\right\}, \tag{4}$$

where $A = 16\pi(G_{\rm N}M)^2$ is the BH area and Euler's constant $\gamma_{\rm E} \approx 0.5772156$. As there are no corrections to the metric, the temperature remains unchanged, and nonlocal quantum corrections yield a pressure P for the BH. The first law of thermodynamics therefore reads

$$T{\rm d}S - P{\rm d}V = \left(1 + \frac{16\pi\,\gamma}{G_{\rm N}M^2}\right){\rm d}M. \tag{5}$$

One identifies $T{\rm d}S = {\rm d}M$ and $16\pi\,\gamma/(G_{\rm N}M^2){\rm d}M = -P{\rm d}V$ with ${\rm d}V = 32\pi G_{\rm N}^3M^2{\rm d}M$, yielding the BH pressure

$$P = -\frac{\gamma}{2G_{\rm N}^4M^4}, \tag{6}$$

which can take negative values, as for spin-0, spin-1/2, and spin-2 fields, one has $\gamma > 0$; or positive values, as $\gamma < 0$ for spin-1 fields. The variation of the nonlocal action (3) yields an effective energy-momentum tensor which has an effective radial pressure component (6), as the nonlocal terms modify the energy equilibrium appearing in the first law of black hole thermodynamics. The identification $T{\rm d}S = {\rm d}M$ therefore continues to hold for the leading-order Bekenstein–Hawking term $S = \frac{A}{4G_{\rm N}}$, representing the dominant entropy contribution, since quantum corrections to the entropy do not alter the thermodynamic differential structure and only shift the internal energy by a small amount already encoded in the work term $P{\rm d}V$. Within the EFT framework, nonlocal corrections act as small backreaction effects encoded in the thermodynamic identity rather than in the spacetime geometry itself [1].

At third order in curvature, the effective action contains a dimension six local operator

$$\mathcal{L}^{(3)} = c_6 G_{\rm N} R^{\mu\nu}{}_{\alpha\sigma} R^{\alpha\sigma}{}_{\beta\rho} R^{\beta\rho}{}_{\mu\nu} \tag{7}$$

where c_6 is a dimensionless parameter corresponding to a Wilson coefficient controlling the first cubic curvature correction in vacuum. There is only one invariant involving only Riemann tensors in vacuum[1], with a corresponding nonlocal operator $R^{\mu\nu}{}_{\alpha\sigma} \log\Box R^{\alpha\sigma}{}_{\beta\rho} R^{\beta\rho}{}_{\mu\nu}$ that can be neglected [28], and cannot be removed by lower-order field redefinitions. In fact, in EFT of gravity, nonlocal terms arise as the low-energy manifestation of 1-loop effects of massless fields and carry additional suppression by inverse powers of the Planck mass. Their contribution to the gravitational action is therefore subleading, compared to the local curvature invariants at the same order in the derivative expansion. Second, for backgrounds of slowly varying curvature, such as the Schwarzschild geometry of a macroscopic black hole, the nonlocal logarithmic operator produces corrections that are proportional to $\log(\Box/\mu^2)$ acting on curvature tensors. In this case, the relevant curvature scales as $R \sim G_{\rm N}M/r^3$, and the $\Box$ operator acts on quantities that vary only over distances of order $r \gg \ell_{\rm PL}$, yielding $\Box R/R \ll M_{\rm PL}^2$. Consequently, the

[1] In the sense that while other cubic curvature invariants exist, in vacuum these reduce to linear combinations of $R^{\mu\nu}{}_{\alpha\sigma} R^{\alpha\sigma}{}_{\beta\rho} R^{\beta\rho}{}_{\mu\nu}$, making c_6 the unique 2-loop vacuum coefficient in pure gravity.

logarithmic kernel produces at most mild, subleading corrections to the local term R^3. Moreover, the nonlocal effects become significant only near or above the cutoff of the EFT, when curvatures approach the Planck scale, or for geometries with rapidly varying fields. Since the EFT description of gravity is valid only for $R/M_{\rm PL}^2 \ll 1$ and for horizon radii much larger than the Planck length ($r_{\rm h} \gg \ell_{\rm PL}$), neglecting the nonlocal $R\log\Box R^2$-type terms at cubic order is self-consistent. This approximation ensures that only the dominant, local dimension-six operator contributes to the leading quantum correction to the Schwarzschild metric (8), with metric coefficients (9).

The dimension six local operator leads to a metric

$$ds^2 = g_{\mu\nu}dx^\mu dx^\nu = -B(r)dt^2 + A(r)dr^2 + r^2 d\Omega^2, \tag{8}$$

with components [1]

$$B(r) = 1 - \frac{2G_{\rm N}M}{r} + 640\pi\, c_6 \frac{G_{\rm N}^5 M^3}{r^7} \tag{9a}$$

$$A(r) = \left[1 - \frac{2G_{\rm N}M}{r} + 3456\pi\, c_6 \frac{G_{\rm N}^4 M^2}{r^6}\left(1 - \frac{49G_{\rm N}M}{27r}\right)\right]^{-1}. \tag{9b}$$

Although the terms that are beyond the usual Schwarzschild solution in Eqs. (9a, 9b) are highly suppressed for astrophysical black holes ($r \gg \ell_{\rm PL}$), they are crucial in providing a well-defined EFT parameterization of short-distance quantum gravity effects. The relation $c_6 G_N \sim 1/M_{\rm PL}^2$ exhibits the canonical EFT suppression by two powers of the reduced Planck mass, reflecting the hierarchy of higher-derivative corrections in low-energy gravity. The coefficient c_6 arises from 2-loop divergences in the Goroff–Sagnotti calculation [28], being a genuine quantum gravitational coupling, rather than a classical higher-curvature ambiguity, and sets the leading nontrivial correction to the vacuum gravitational action in the EFT expansion.

In pure Einstein gravity, the 1-loop effective action is finite on shell, but Goroff and Sagnotti [28] showed that at two loops the effective action develops a divergence proportional to the same cubic invariant

$$\Gamma^{(2)}_{\rm div} = \frac{209}{2880(4\pi)^4\epsilon}\int {\rm d}^4x\sqrt{|g|}\, R^{\mu\nu}{}_{\alpha\sigma} R^{\alpha\sigma}{}_{\beta\rho} R^{\beta\rho}{}_{\mu\nu}. \tag{10}$$

The numerical factor in Eq. (10) is the canonical Goroff–Sagnotti coefficient that multiplies the 2-loop counterterm in pure Einstein gravity [28]. The term $\epsilon = 4 - d$ is the standard parameter employed in the dimensional regularization procedure, where calculations are performed in d spacetime dimensions and the result, as usual, is expanded around $d = 4$, to isolate the divergent parts. This divergence is absorbed by the counterterm c_6, leaving a finite, renormalized coefficient

$$c_6(\mu) = c_6^{\rm BARE} + \frac{209}{2880(4\pi)^4}\frac{1}{\epsilon} + c_6^{\rm FINITE}(\mu), \tag{11}$$

where $c_6^{\rm FINITE}(\mu)$ depends on the renormalization scale μ and the ultraviolet (UV) completion of gravity. Therefore, the coefficient c_6 can be thought of as the finite part of a loop counterterm absorbing the Goroff–Sagnotti divergence. The coefficient c_6 runs logarithmically with μ, according to the equation $\mu\frac{{\rm d}c_6}{{\rm d}\mu} = \beta_{c_6}$, where β_{c_6} is the renormalization group beta function computable from loop diagrams, indicating how the coefficient c_6 runs as one probes gravity at different energies. The dependence on the renormalization scale encodes how the UV description of gravity feeds into low-energy predictions for higher-curvature effects.

It is worth noting that gravitational theories containing higher-derivative operators, such as the cubic curvature term (7), are generically subject to the Ostrogradsky instability, which arises from the presence of higher-order time derivatives in the action and typically indicates the existence of ghostlike degrees of freedom [69,70], including the case with unsuppressed cubic curvature terms [31]. Within the EFT framework adopted here, however, these operators are treated perturbatively as higher-order corrections suppressed by powers of the Planck scale, ensuring that no additional propagating degrees of freedom appear below the cutoff. The would-be ghost poles associated with the higher-derivative terms lie far above the EFT validity range and therefore do not correspond to physical excitations in the low-energy regime. Consequently, the EFT remains consistent with GR as the deep-infrared and lowest-energy approximation, with the higher-curvature terms encoding virtual quantum gravitational effects rather than introducing new dynamical fields [65,71,72]. This interpretation is consistent with the standard treatment of quadratic and cubic curvature corrections in the EFT of gravity [1,64,68,73,74], where higher-order operators parameterize nonlocal quantum effects and remain under perturbative control.

Other quantum gravitational corrections from the dimension-six operator describing stellar distributions have been studied in Ref. [75].

3 Quantum gravitational corrected black holes and the de Laval nozzle

This section explores the conditions under which sound waves propagating through a fluid in a de Laval nozzle can emulate bosonic (massless scalar fields, electromagnetic fields, and axial gravitational perturbations) and fermionic (Dirac) field perturbations on the quantum-corrected metric (8). Specifically, the focus is on the QN ringing modes. Perturbations in an actual BH often lead to the emission of GWs, characterized by an initial blast of strong-field radiation, followed by a phase of damped oscillations dominated by QN modes. The QN modes are fingerprints of the BH

geometry and are pivotal for understanding its underlying stability and dynamics.

The relativistic equations for massless scalar fields Φ, electromagnetic fields A_μ, and Dirac fields ψ in a background described by the quantum gravitational metric $g_{\mu\nu}$ in Eq. (8), with coefficients (9), can be respectively expressed as

$$\frac{1}{\sqrt{-g}}\partial_\mu\left(\sqrt{-g}g^{\mu\nu}\partial_\nu\right)\Phi\left(x^\mu\right)=0, \tag{12a}$$

$$\frac{1}{\sqrt{-g}}\partial_\mu\left(F_{\rho\sigma}g^{\mu\rho}g^{\tau\sigma}\sqrt{-g}\right)=0, \tag{12b}$$

$$\gamma^\alpha e_\alpha^{\ \mu}\left(\partial_\mu-\gamma_\mu\right)\psi\left(x^\mu\right)=0, \tag{12c}$$

where $g=\det\left(g_{\mu\nu}\right)$, $F_{\mu\nu}=\partial_\mu A_\nu-\partial_\nu A_\mu$, γ^α are the Dirac matrices, $\gamma_\mu=-\frac{1}{8}\left[\gamma^\rho,\gamma^\sigma\right]g_{\alpha\tau}e_\rho^{\ \alpha}\nabla_\mu e_\sigma^{\ \tau}$ denotes the spin connection, and $e_\mu^{\ \nu}$ stands for the tetrad field which expressed the metric $g_{\mu\nu}$ in terms of the Minkowski metric $\eta_{\mu\nu}$ by $g_{\mu\nu}=\eta_{\lambda\sigma}e_\mu^{\ \lambda}e_\nu^{\ \sigma}$.

The first step to compute QN modes is to introduce a tortoise coordinate for the quantum-corrected BH metric (8),

$$\frac{\mathrm{d}r_\star}{\mathrm{d}r}=\sqrt{\frac{A(r)}{B(r)}}. \tag{13}$$

The perturbations can be decomposed in modes of frequency ω, to wit

$$\Phi\left(t,r_\star,\theta,\varphi\right)=e^{-i\omega t}\frac{R(r_\star)}{r_\star}Y_\ell^m\left(\theta,\varphi\right), \tag{14}$$

where spherical harmonics of degree ℓ and order m are given by

$$Y_\ell^m\left(\theta,\varphi\right)=\frac{\left(\sin\theta\right)^{|m|}}{2^\ell\ell!}\left(\frac{\mathrm{d}}{\mathrm{d}\cos\theta}\right)^{|m|+\ell}\left(1-\cos^2\theta\right)^{-\ell}e^{im\varphi}. \tag{15}$$

Equations (12a)-(12c) then reduce to a Schrödinger-like differential eq [39,42,53]

$$\left(\frac{\mathrm{d}^2}{\mathrm{d}r_\star^2}+\omega^2-V_{\mathrm{EFF}}(r_\star)\right)R(r_\star)=0, \tag{16}$$

for the radial part $R(r_\star)$. The effective potential, respectively for integer and semi-integer values of the spin, reads:

$$V_{\mathrm{EFF}}(r)=\begin{cases}B(r)\dfrac{\ell\left(\ell+1\right)}{r^2}+\dfrac{1-s^2}{2r}\dfrac{\mathrm{d}}{\mathrm{d}r}\left(\dfrac{B\left(r\right)}{A\left(r\right)}\right), & \text{for } s\in\mathbb{Z},\\[2ex] \dfrac{B(r)}{r^2}\left(\ell+\dfrac{1}{2}\right)^2\pm\left(\ell+\dfrac{1}{2}\right)\sqrt{\dfrac{B(r)}{A(r)}}\dfrac{\mathrm{d}}{\mathrm{d}r}\left(\dfrac{\sqrt{B\left(r\right)}}{r}\right), & \text{for } s\in\mathbb{Z}+\dfrac{1}{2}.\end{cases} \tag{17}$$

The Dirac field is governed by two isospectral wave functions, which can be transformed into one another using the Darboux transformation [76]. Hence, choosing only $V_{\mathrm{EFF}}^{+}(r)$, corresponding to the positive sign on the right-hand side of the second equation in (17) is sufficient for the analysis of QN modes [77**?**].

The effective potential for integer spins, calculated with the quantum corrected Schwarzschild Metric, Eq. (9), can be written in terms of the parameter c_6 as follows:

$$V_{\mathrm{EFF}}^{\mathrm{bosonic}}(r)=V_0(r)+V_1(r)c_6+V_2(r)c_6^2, \tag{18}$$

where $V_0(r)$ is the effective potential for the Schwarzschild metric, whereas $V_1(r)$ and $V_2(r)$ are corrections coupled with c_6 and c_6^2, respectively:

$$V_0(r)=\left(1-\frac{2G_NM}{r}\right)\left(\frac{\ell\left(\ell+1\right)}{r^2}-\frac{2G_NM}{r^3}\left(s^2-1\right)\right) \tag{19a}$$

$$V_1(r)=\left[640\frac{G_NM}{r}\ell\left(\ell+1\right)+\left(10368-43904\frac{G_NM}{r}+45056\frac{G_N^2M^2}{r^2}\right)\left(s^2-1\right)\right]\frac{G_N^4M^2}{r^8}\pi \tag{19b}$$

$$V_2(r)=\left(14376960-28098560\frac{G_NM}{r}\right)\left(s^2-1\right)\frac{G_N^9M^5}{r^{15}}\pi^2. \tag{19c}$$

The quadratic structure of Eq. (18) shows that integer-spin particles sense the quantum correction up to c_6^2. It is now easy to see that the effective potential saturates with the parameter

$$c_6^{\mathrm{saturation}}=-\frac{1}{2}\frac{V_1(r)}{V_2(r)}. \tag{20}$$

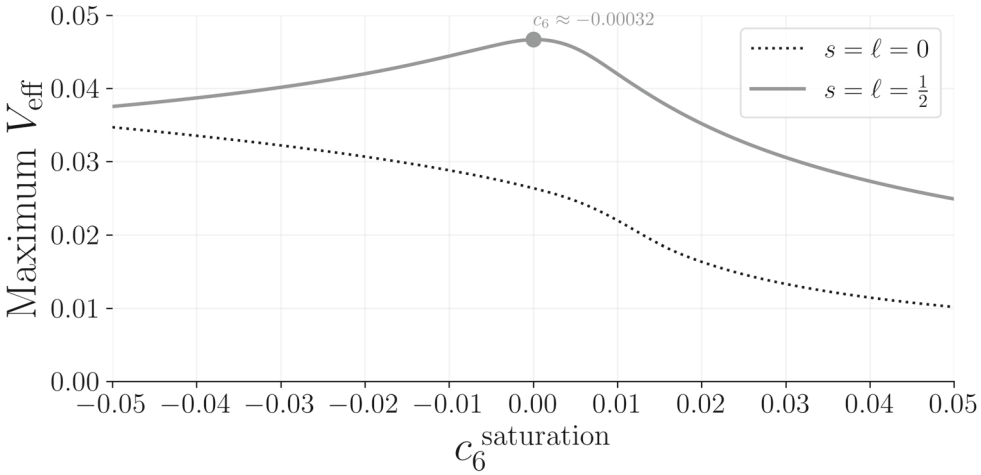

Fig. 1 Saturation value for c_6 that maximises V_{eff}, versus its maximum effective potential value. The circle represents the global maximum value. The dotted black line considers $s = \ell = 0$, whereas the solid grey line considers $s = \ell = 1/2$. Values calculated with natural units and $M = 1$

The effective potential for particles with spin-1/2 is given by

$$V_{\text{EFF}}^{\text{fermionic}}(r) = \frac{1}{r^2}\left(\ell + \frac{1}{2}\right)^2 \left(1 - \frac{2G_{\text{N}}M}{r} + 640\pi c_6 \frac{G_{\text{N}}^5 M^3}{r^7}\right) - \frac{1}{r^2}\left(\ell + \frac{1}{2}\right)\sqrt{1 - \frac{2G_{\text{N}}M}{r} + 3456\pi\, c_6 \frac{G_{\text{N}}^4 M^2}{r^6}\left(1 - \frac{49G_{\text{N}}M}{27r}\right)} \times \left(1 - \frac{3G_{\text{N}}M}{r} + 2880\pi c_6 \frac{G_{\text{N}}^5 M^3}{r^7}\right). \tag{21}$$

Different from the integer case, $V_{\text{EFF}}^{\text{fermionic}}(r)$ is not a polynomial in c_6, and thus this case should be more sensitive to quantum corrections. To compare the two cases, the saturation values of c_6 and the maximum value of $V_{\text{EFF}}(r)$ can be analysed. Figure 1 shows the value of c_6 that saturates $V_{\text{EFF}}(r)$, and its value. Figure 2 shows the orbit radius r_{orbit}, varying c_6 from -0.05 to 0.05. The fermionic trajectory in Fig. 1 exhibits non-monotonic behaviour: as $c_6 \lesssim 0$, $V_{\text{eff}}^{\max}$ increases with c_6, and when $c_6 \gtrsim 0$, $V_{\text{eff}}^{\max}$ decreases with c_6, faster than the bosonic case. This behaviour will be present in the results in Sect. 4. It is important to point out that $V_{\text{EFF}}^{\text{fermionic}}(r)$ reaches its global maximum value near Schwarzschild, so spin-1/2 particles experience the maximum attraction when $c_6 \approx 0$ and rapidly change with a small quantum perturbation, with bigger slopes near Schwarzschild (minimum global slope value ≈ -0.722 at $c_6 \approx 0.01$ and maximum global slope value ≈ 0.264 at $c_6 \approx -0.01$).

The integer spin case is less sensitive to variations of c_6. The curve is monotonic, so as c_6 increases, $V_{\text{eff}}^{\max}$ decreases. The behaviour only changes with higher values for c_6, for which no maximum $V_{\text{eff}}^{\max}$ can be defined. For reasonable values of c_6, the bosonic curve shown in Fig. 1 does not have a well-defined global maximum or minimum. Similar to the fermionic case, the minimum global slope is located at $c_6 \approx 0.01$ with value ≈ -0.592.

Fig. 2 shows that fermionic orbits are closer to the event horizon than the bosonic case, in every c_6 value. The minimum stable orbit, for either the fermionic or the bosonic case, is reached with $c_6 \neq 0$, so one can expect a setup different from the Schwarzschild metric that minimises the total energy of the system, and thus preferred by nature.

To establish the connection with BH perturbations and fluid dynamics, one can express the Navier–Stokes equations for a longitudinal horizontal de Laval nozzle as [61]

$$\rho\left[\frac{\partial \mathbf{u}}{\partial t} + \left(\mathbf{u}\cdot\nabla\right)\mathbf{u}\right] = -\nabla p - \rho\nabla\Phi + \eta\nabla^2\mathbf{u} + \left(\xi + \frac{1}{3}\eta\right)\nabla\left(\nabla\cdot\mathbf{u}\right). \tag{22}$$

Eq. (22) describes the dynamics of a viscous heat-conducting fluid flow, with flow velocity profile $\mathbf{u} = \mathbf{u}(x^\mu)$, where η is the dynamic shear viscosity, ξ represents the bulk viscosity, $\rho = \rho(x^\mu)$ denotes the fluid density, and $\Phi = \Phi(x^\mu)$ is a scalar potential. These equations are reduced to the Euler equations in the absence of viscosity. Isentropic flows are both adiabatic and reversible, meaning that no heat is added to the fluid flow, even those due to friction or dissipative effects. For isentropic flows, the flow velocity field can be expressed as $\mathbf{u} = -\nabla\varphi$, where φ is the velocity potential. Under these assumptions, the equations ruling the fluid flow are simplified to:

$$\frac{\partial(\rho \mathrm{A})}{\partial t} + \nabla\cdot(\rho \mathrm{A}\mathbf{u}) = 0, \tag{23a}$$

$$-\frac{\partial\varphi}{\partial t} + h + \frac{1}{2}(\nabla\varphi)^2 + \Phi = 0, \tag{23b}$$

where A denotes the cross-sectional area of a de Laval nozzle, and h represents the specific enthalpy, encoding the internal energy of the fluid flow and the product of its pressure and volume per unit mass. To investigate wave dynamics within

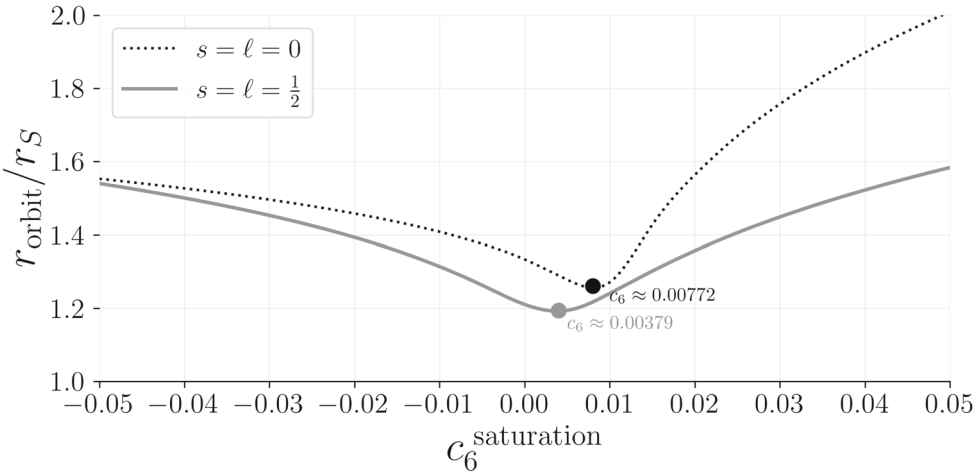

Fig. 2 Saturation value for c_6 that maximises $V_{\rm eff}$, versus the orbital radius value relative to the Schwarzschild Radius $r_S = 2G_{\rm N}M$. The circles represent the global minimum value for each combination of s and ℓ. The dotted black line considers $s = \ell = 0$, whereas the solid grey line considers $s = \ell = 1/2$

this setup, applying perturbations to Eqs. (23a) and (23b) yields

$$-\frac{\partial}{\partial t}\left\{\frac{\rho \mathrm{A}}{c_{\mathrm{S}}^2}\left[\frac{\partial(\delta\varphi)}{\partial t}+\mathbf{u}\cdot\left(\nabla(\delta\varphi)\right)\right]\right\} +\nabla\cdot\left\{\rho \mathrm{A}\nabla(\delta\varphi)-\left\{\frac{\rho \mathrm{A}}{c_{\mathrm{S}}^2}\left[\frac{\partial(\delta\varphi)}{\partial t}+\mathbf{u}\cdot\left(\nabla(\delta\varphi)\right)\right]\right\}\mathbf{u}\right\}=0, \tag{24}$$

where $c_{\rm S}$ is the speed of sound in the medium.

The Venturi effect governs the behavior of fluid flows within de Laval nozzles. In inviscid fluid dynamics, the velocity of a fluid flow must rise as it flows through the nozzle constriction, according to mass conservation. In contrast, the fluid flow static pressure must decrease by the Bernoulli principle and the Euler equations. Therefore, any increase in kinetic energy that the fluid experiences due to its increased velocity through a constriction is counterbalanced by a reduction in pressure resulting from a decrease in potential energy. When a fluid passes through a constricted region of a tube with varying cross-sectional area $\mathrm{A}(x)$, the pressure decreases while the velocity increases. The mass flow rate for a compressible fluid increases as the upstream pressure increases, yielding the increment of the fluid density through the nozzle constriction, although the flow velocity remains unaltered. This is the principle governing de Laval nozzles. The higher the source temperature, the higher the local sonic velocity is, permitting the mass flow rate to increase. However, it occurs only if the de Laval nozzle area also increases, to compensate for the resulting decrement in density. For an ideal gas under non-viscous, adiabatic, and isentropic conditions, the equation of state $p = \rho RT$ applies, where T represents the fluid temperature and $R = 8.3144\ \mathrm{JK}^{-1}\ \mathrm{mol}^{-1}$ denotes the ideal gas constant. Key thermodynamic properties of the gas include its heat capacities at constant pressure ($c_{\rm P}$) and constant volume ($c_{\rm V}$), related by $R = c_{\rm P} - c_{\rm V}$. The adiabatic index $\gamma = c_{\rm P}/c_{\rm V}$ characterizes the fluid flow, as the speed of sound depends on this factor. Isentropic flows satisfy the relation

$$p = \rho^{\gamma} = T^{\frac{\gamma}{\gamma-1}}, \tag{25}$$

ensuring shock-free and continuous flow properties.

The Mach number, $\mathrm{M}(x) = \left|\mathbf{u}(x)\right|/c_{\rm S}(x)$, is a dimensionless parameter that quantifies the flow velocity ratio to the local speed of sound, with $c_{\rm S}^2 = \mathrm{d}p/\mathrm{d}\rho = \gamma RT$ representing the speed of sound. Here, x denotes the longitudinal coordinate along the convergent-divergent nozzle. The mass flux $\mathrm{d}m/\mathrm{d}t \equiv \dot{m}$ measures the rate at which mass flows through the nozzle cross-section per unit of time and must be constant to ensure the continuity equation derived from mass conservation. Assuming that the nozzle radius $r = r(x)$ varies gradually along x, perturbations in the fluid flow can be approximated as quasi-one-dimensional ones, and we can write $\mathbf{u} = u\hat{\imath}$. Under these assumptions, Eq. (24) simplifies to describe scalar field perturbations along a single propagation direction:

$$\left[\left(\frac{\partial}{\partial t}+\frac{\partial u}{\partial x}\right)\frac{\rho \mathrm{A}}{c_s^2}\left(\frac{\partial}{\partial t}+u\frac{\partial}{\partial x}\right)-\frac{\partial}{\partial x}\left(\rho \mathrm{A}\frac{\partial}{\partial x}\right)\right]\delta\varphi=0. \tag{26}$$

Analogous to the QN modes described in Eq. (16), stationary solutions can be expressed through a Fourier transform

$$\delta\varphi(x,t)=\frac{1}{2\pi}\int \mathrm{d}\omega e^{-i\omega t}\delta\varphi_\omega(x). \tag{27}$$

Substituting this into Eq. (26) results in a time-independent differential equation for $\delta\varphi_\omega$, expressed as

$$\frac{1}{2\pi}\int \mathrm{d}\omega e^{-i\omega t}\left\{\rho\mathrm{A}\left(1-\frac{u^2}{c_\mathrm{S}^2}\right)\frac{\mathrm{d}[}{\mathrm{d}2}]x+\left[\frac{\mathrm{d}(\rho\mathrm{A})}{\mathrm{d}x}\right.\right.$$
$$+2i\omega\frac{\rho\mathrm{A}u}{c_\mathrm{S}^2}-\frac{\mathrm{d}}{\mathrm{d}x}\left(\frac{\rho\mathrm{A}u^2}{c_\mathrm{S}^2}\right)\Bigg]\frac{\mathrm{d}}{\mathrm{d}x}$$
$$\left.+\left[\omega^2\frac{\rho\mathrm{A}}{c_\mathrm{S}^2}+i\omega\frac{\mathrm{d}}{\mathrm{d}x}\left(\frac{\rho\mathrm{A}u}{c_\mathrm{S}^2}\right)\right]\right\}\delta\varphi_\omega=0. \tag{28}$$

To simplify the analysis, auxiliary quantities can be introduced, such as the transfer function [57–59]

$$F_\omega(x)=\sqrt{g_\mathrm{C}}\int \mathrm{d}t\exp\left\{i\omega\left[t-\int \mathrm{d}x\frac{u}{(c_s^2-u^2)}\right]\right\}$$
$$\delta\varphi(t,x), \tag{29}$$

where $g_\mathrm{C}=\rho\mathrm{A}/c_\mathrm{S}$. Additionally, a coordinate transformation $x=x(x_\star)$ based on the tortoise coordinate for the canonical acoustic BH can be applied:

$$\frac{\mathrm{d}x_\star}{\mathrm{d}x}=\frac{c_{\mathrm{S}0}}{c_\mathrm{S}(1-\mathrm{M}^2)}, \tag{30}$$

where $c_{\mathrm{S}0}$ represents the stagnation sound speed, and $x_\star$ serves as the acoustic analog of the tortoise coordinate. Under these transformations, Eq. (28) assumes the form of a Schrödinger-wavelike differential equation:

$$\left(\frac{\mathrm{d}^2}{\mathrm{d}x_\star^2}+\frac{\omega^2}{{c_{\mathrm{S}0}}^2}-V_{\mathrm{EFF}}(x_\star)\right)F_\omega(x_\star)=0, \tag{31}$$

with the effective potential given by [59]

$$V_{\mathrm{EFF}}(x_\star)=\frac{1}{2g_\mathrm{C}}\frac{\mathrm{d}g_\mathrm{C}^2}{\mathrm{d}x_\star^2}-\left(\frac{1}{2g_\mathrm{C}}\frac{\mathrm{d}g_\mathrm{C}}{\mathrm{d}x_\star}\right)^2. \tag{32}$$

With the equations and effective potentials for both gravitational and aerodynamic systems now established, the next step involves their application in experimental contexts. First, a precise relationship between the fluid density ρ and the parameter g_C must be determined. Subsequently, the constraint equations linking the Schrödinger-wavelike equations – Eq. (16) for gravitational QN modes and the dual analog Eq. (31) for acoustic BHs – must be analyzed to fully understand the QN mode dynamics in both analog systems.

To ensure consistency between the wave dynamics described by Eq. (31) and the effective potential in Eq. (32), it is convenient to express the de Laval nozzle cross-sectional area A in terms of g_C. For a perfect fluid under isentropic flow conditions, the nozzle longitudinal area A relative to the area at the nozzle throat $\mathrm{A}_\star$ can be described by

$$\frac{\mathrm{A}}{\mathrm{A}_\star}=\frac{1}{\mathrm{M}}\left[\frac{2}{\gamma+1}\left(1+\frac{\gamma-1}{2}\mathrm{M}^2\right)\right]^{\frac{\left(\gamma+1\right)}{2(\gamma-1)}}, \tag{33}$$

Remembering that M represents the Mach number and γ is the adiabatic index.

To simplify the analysis, hereon both A and ρ are normalized by their respective throat values, $\mathrm{A}_\star$ and ρ_0. Using these normalized quantities, one can express:

$$g_\mathrm{C}=\frac{1}{2}\rho^{(3-\gamma)/2}\mathrm{A}, \tag{34a}$$
$$\mathrm{A}^{-1}=\rho\sqrt{1-\rho^{(\gamma-1)}}. \tag{34b}$$

The density ρ can be related to g_C as:

$$\rho^{1-\gamma}=2g_\mathrm{C}^2\left(1-\frac{\sqrt{g_\mathrm{C}^2-1}}{g_\mathrm{C}}\right). \tag{35}$$

Substituting this into the expression for A yields:

$$\mathrm{A}=\sqrt{2g_\mathrm{C}\left(\sqrt{g_\mathrm{C}^2-1}+g_\mathrm{C}\right)}\left[2g_\mathrm{C}^2\left(1-\sqrt{1-g_\mathrm{C}^{-2}}\right)\right]^{\frac{1}{\gamma-1}}. \tag{36}$$

Using the relationships between local and total quantities for isentropic flows with Eq. (34a) yields

$$\rho^{-1}=\left(1+\frac{\gamma-1}{2}\mathrm{M}^2\right)^{\frac{1}{\gamma-1}}, \tag{37}$$

implying that

$$g_\mathrm{C}=\frac{1}{\mathrm{M}\sqrt{2(\gamma-1)}}\left(1+\frac{\gamma-1}{2}\mathrm{M}^2\right), \tag{38}$$

where $\mathrm{M}=1$ at the event horizon r_H, corresponding to the nozzle throat. For air flow ($\gamma\approx 1.40$), g_C satisfies:

$$g_\mathrm{C}(r_\mathrm{H})=\frac{\gamma+1}{2\sqrt{2(\gamma-1)}}=\frac{3\sqrt{5}}{5}>1. \tag{39}$$

This condition provides a boundary constraint for numerical integrations. The second boundary constraint is

$$\lim_{r\to r_\mathrm{H}}\frac{\mathrm{dA}}{\mathrm{d}x}=0, \tag{40}$$

or, equivalently,

$$\lim_{r\to r_\mathrm{H}}\frac{\mathrm{d}g_\mathrm{C}}{\mathrm{d}x}=0, \tag{41}$$

indicating that the nozzle geometry is smooth at the throat.

The Schrödinger-type Eqs. (16) and (31) are derived from an effective potential and the tortoise coordinate framework. Establishing the equivalence between the effective potentials

requires the tortoise coordinates from both systems to be equal, leading to the condition

$$\mathrm{d}r_\star = \mathrm{d}x_\star = \sqrt{\frac{A(r)}{B(r)}}\mathrm{d}r = \frac{\Big(\gamma-1\Big)\sqrt{2g_{\rm C}^2\Big(1-\sqrt{1-g_{\rm C}^{-2}}\Big)}}{\gamma+1-4g_{\rm C}^2\Big(1-\sqrt{1-g_{\rm C}^{-2}}\Big)}\mathrm{d}x. \tag{42}$$

By defining $\mathrm{F}(r) \equiv \sqrt{B(r)/A(r)}$, this relation simplifies to [59]

$$\frac{\mathrm{d}x}{\mathrm{d}r} = \frac{\gamma+1-4g_{\rm C}(r)^2\Big(1-\sqrt{1-g_{\rm C}(r)^{-2}}\Big)}{\mathrm{F}(r)\Big(\gamma-1\Big)\sqrt{2g_{\rm C}(r)^2\Big(1-\sqrt{1-g_{\rm C}(r)^{-2}}\Big)}}. \tag{43}$$

The function $g_{\rm C}(r)$ can be determined by rewriting the effective potential, Eq. (32), as

$$\frac{g_{\rm C}''(r)}{g_{\rm C}(r)} + \frac{g_{\rm C}'(r)}{g_{\rm C}(r)}\left(\frac{\mathrm{F}'(r)}{\mathrm{F}(r)} - \frac{1}{2}\frac{g_{\rm C}'(r)}{g_{\rm C}(r)}\right) = \frac{2V_{\rm EFF}(r)}{\mathrm{F}^2(r)}. \tag{44}$$

Singularities in solving this equation are resolved via the substitution $g_{\rm C}(r) \equiv \chi^2(r)$, yielding:

$$\chi''(r) + \frac{\mathrm{F}'(r)}{\mathrm{F}(r)}\chi'(r) - \frac{V_{\rm EFF}(r)}{\mathrm{F}^2(r)}\chi(r) = 0. \tag{45}$$

Eq. (45) has the appropriate form to apply the Frobenius method. For the Schwarzschild limit ($c_6 \to 0$), the solution reduces to:

$$g_{\rm C} = \frac{\gamma+1}{2\sqrt{2}\sqrt{\gamma-1}} \left[\frac{\Gamma(1+\ell+s)\,{}_2F_1\Big(s-\ell, s+\ell+1, 1+2s, \frac{r}{2G_{\rm N}M}\Big)}{(2s)!(\ell-s)!} \left(\frac{r}{2G_{\rm N}M}\right)^{s+1}\right]^2, \tag{46}$$

consistent with prior results [59]. Near the horizon $r_{\rm H}$, the Frobenius method is applied using the series expansion

$$\chi\Big(r\Big) = \sum_{k=0}^{\infty} a_k\Big(r-r_{\rm H}\Big)^{k+p}, \tag{47}$$

with indicial conditions

$$a_0 = \sqrt{\frac{\gamma+1}{2\sqrt{2}\sqrt{\gamma-1}}}, \quad a_1 = 0. \tag{48}$$

It generates the recurrence relation

$$\Big(k+2\Big)\Big(k+1\Big)a_{k+2} + \Big(k+1\Big)a_{k+1}\frac{\mathrm{F}'(r)}{\mathrm{F}(r)} - a_k\frac{V_{\rm EFF}(r)}{\mathrm{F}^2(r)} = 0, \tag{49}$$

which leads to

$$g_{\rm C}\Big(r\Big) = \frac{\gamma+1}{2\sqrt{2}\sqrt{\gamma-1}}\left[1+\frac{1}{2}\frac{V_{\rm EFF}(r)}{\mathrm{F}^2(r)}\Big(r-r_{\rm H}\Big)^2 - \frac{1}{6}\frac{V_{\rm EFF}(r)}{\mathrm{F}^2(r)}\frac{\mathrm{F}'(r)}{\mathrm{F}(r)}\Big(r-r_{\rm H}\Big)^3 + \cdots\right]^2. \tag{50}$$

Numerical integration via Runge–Kutta methods then determines $g_{\rm C}(r)$, which is subsequently mapped to the nozzle longitudinal coordinate x using Eq. (43). This setup applies to the quantum-corrected metric (8), for analyzing analog quantum-corrected nozzle profiles and their QN modes.

4 De Laval nozzle analog of quantum gravitational corrected black holes, QN modes and their overtones

The analogy between sound waves in a de Laval nozzle and quantum-corrected BHs (8) goes beyond qualitative comparisons, allowing for quantitative analysis within experimental precision. This enables the examination of fluid flow propagation features in de Laval nozzles with numerical accuracy. QN modes, described by the wave eq (16) in gravitational systems and by Eq. (31) for acoustic BHs, demonstrate a numerical correspondence. This equivalence implies that the effective potential governing perturbations in a specific aerodynamic configuration matches that of quantum gravitational corrected BHs. Consequently, acoustic waves in de Laval nozzles create an analog physical system replicating the effective potential generating QN modes by perturbations of quantum-gravitational corrected BHs.

4.1 The quantum gravitational corrected analog de Laval nozzle

To solve numerically Eq. (45) requires fixing the value of the parameter c_6 in the components (9), alongside the spin s and multipole quantum number ℓ in Eq. (17). The parameter c_6, corresponding to third-order curvature corrections in the effective field theory, must satisfy $|c_6| \lesssim \mathcal{O}(1)$ to preserve perturbative validity [1]. For astrophysical BHs ($M \gg M_{\rm PL}$), values beyond this limit violate the consistency of the effective field theory, while Planck-scale systems ($M \sim M_{\rm PL}$) require renormalization group analysis to relate c_6 to the the renormalization scale μ [1]. The wave modes are classified by the multipole quantum number ℓ. We have $\ell = 0$ (s-wave, spherically symmetric perturbations), $\ell = 1$ (p-wave,

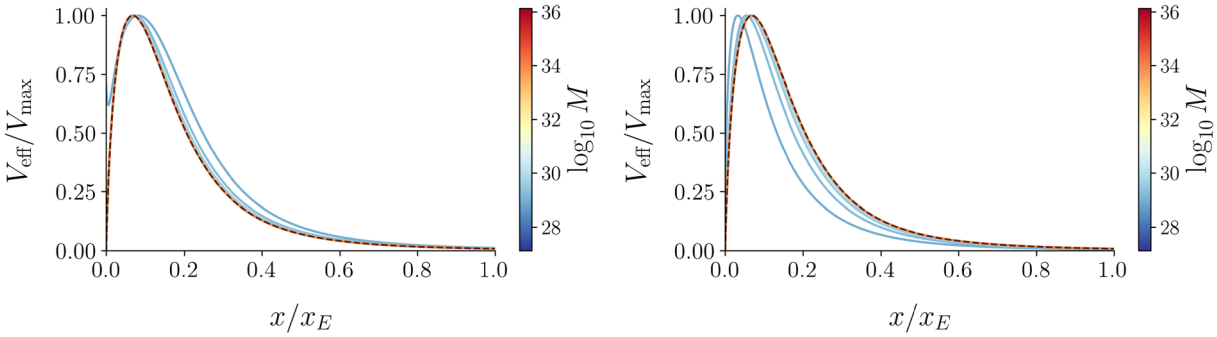

(a) $s = \ell = 0$, $c_6 = 0.005$. (b) $s = 0$ and $\ell = 0$, $c_6 = -0.01$.

Fig. 3 Effective potential as a function of the longitudinal direction of the de Laval nozzle, varying the BH mass in the range 10^{27} kg $< M < 10^{36}$ kg and keeping c_6 fixed

dipole axial oscillations), $\ell = 2$ (d-wave, quadrupole gravitational modes), $\ell = 1/2$ (fermionic s-wave, spin-1/2 field excitations), and $\ell = 3/2$ (fermionic p-wave, spin-1/2 field excitations).

The metric (8) imposes constraints on c_6 through the corrected event horizon radius:

$$r_{\rm H} = 2G_{\rm N}M\left(1 - c_6\frac{5\pi}{G_{\rm N}^2M^4}\right), \tag{51}$$

which requires $c_6 < \mathcal{O}(G_{\rm N}^2M^4/\pi)$ to ensure $r_{\rm H} \in \mathbb{R}^+$. For $M \sim M_{\rm PL}$, this simplifies to the reasonable $|c_6| \leq 1$. Numerical solutions of Eqs. (43) and (45) are therefore restricted to $|c_6| \leq 1$, avoiding unphysical horizons or divergent potentials. More precisely, Eq. (51) implies that $c_6 \ll G_{\rm N}^2M^4/5\pi$, for all possible values of the BH mass M in units with $G_{\rm N} = 1/M_{\rm PL}^2$. Since the minimum admissible BH mass has order $M \sim M_{\rm PL}$, and as the parameter driving quantum gravitational corrections is assumed to be independent of M, the quantum gravitational correction parameter c_6 can be constrained using $M \sim M_{\rm PL}$, yielding the bound

$$|c_6| < \frac{1}{5\pi} \sim 0.0636. \tag{52}$$

The de Laval nozzle characteristics are analyzed as functions of the quantum-correction parameter c_6, with spin configurations $s = 0, 1, 2, 1/2$ and multipole numbers $\ell = s + n$, for $n \in \mathbb{N}$. More precisely, spinor, scalar, vector, and tensor perturbations of fluid flows in analog aerodynamics are proposed to experimentally probe QN modes of quantum gravity-corrected BHs, also for distinct overtones.Figuers. 3a and 3b illustrate the effective potential $V_{\rm EFF}$ as a function of the longitudinal coordinate in the de Laval nozzle (normalized by the total length $x_{\rm E}$ of the nozzle), evaluated for distinct stellar and astrophysical masses varying systematically in the range 10^{27} kg $< M < 10^{36}$ kg. The parameter c_6, regulating quantum gravity corrections, is chosen to obey the constraint (52). Scalar s-wave perturbations, given by $s = \ell = 0$ are shown in Figs. 3a and 3b

Figure. 3a considers the positive value $c_6 = 0.005$ and shows that the effective potential starts to decay, after the peak, at higher values of the longitudinal coordinate x, for astrophysical objects with masses around the Solar mass, although their asymptotic values remain very similar. On the other hand, Fig. 3b regards the negative value $c_6 = -0.01$, illustrating the behaviour of the effective potential, this time decaying at lower values of the longitudinal coordinate x, for stellar objects with masses around the Solar mass. Similarly to Fig. 3a Figs. 3a and 3b corroborate the fact that the effect of c_6 reduces for increasing masses. They also show that quantum gravitational effects essentially disappear for values of the BH mass higher than Solar masses. It means that quantum gravity corrections are potentially discernible in primordial BHs.

The thermodynamic variables, the nozzle geometry, the Mach number, and the thrust coefficient are computed as functions of c_6. Calculations of QN modes incorporate spin and multipole values, which are critical for overtone analysis and for the calculation of the quality factor $q_n \sim \Re(\omega)/\Im(\omega)$. The QN mode spectrum is computed for various values of c_6. Eq (9), (17) and (51) reveal that solutions with $c_6 \geq G_{\rm N}^2M^4/5\pi$ yield non-physical solutions, as they either do not provide a real event horizon radius $r_{\rm H}$ or the effective potentials $V_{\rm EFF}$ associated with them are not well behaved. Consequently, all subsequent results in Figs. 4–10 are generated for fixed values of s and ℓ, while c_6 is varied systematically. The nozzle throat center at $x = 0$ corresponds to the analog event horizon in these configurations. To simplify the analysis, from now on we consider natural units with unitary BH mass, $G_{\rm N} = M = 1$.

Figure 4 displays the effective potential $V_{\rm EFF}$ as a function of the longitudinal coordinate in the de Laval nozzle, evaluated for distinct values of the parameter c_6 driving quantum gravity corrections, spin s, and multipole ℓ. Scalar s-

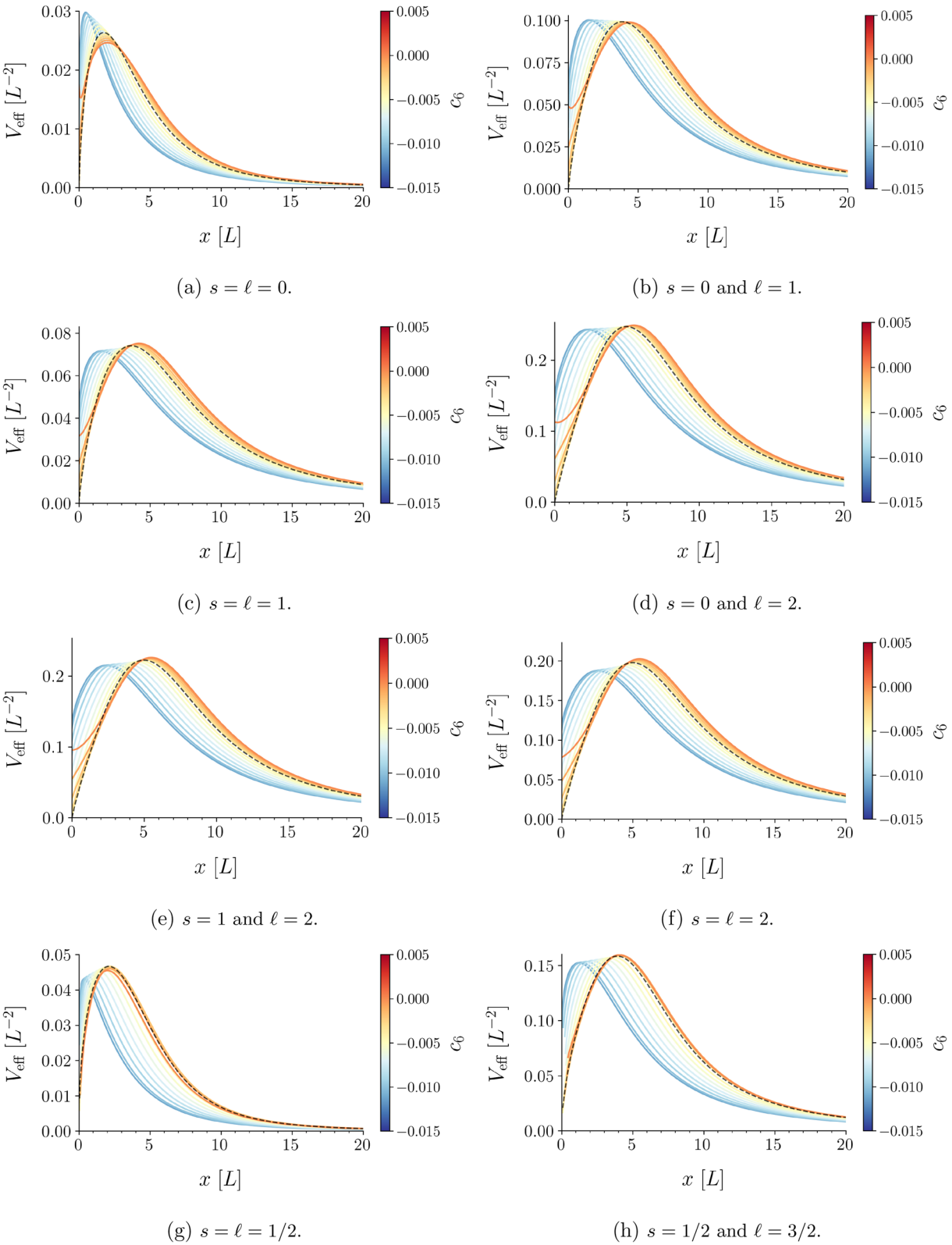

(a) $s = \ell = 0$. (b) $s = 0$ and $\ell = 1$.

(c) $s = \ell = 1$. (d) $s = 0$ and $\ell = 2$.

(e) $s = 1$ and $\ell = 2$. (f) $s = \ell = 2$.

(g) $s = \ell = 1/2$. (h) $s = 1/2$ and $\ell = 3/2$.

Fig. 4 Effective potential as a function of the longitudinal direction of the de Laval nozzle, varying c_6 for the quantum-corrected Schwarzschild metric (8). The dashed black line represents the Schwarzschild solution. The values are calculated using $G_{\text{N}} = M = 1$

wave perturbations, given by $s = \ell = 0$, are shown in Fig. 4a and 4c – 4f and 4h Variations in c_6 modulate the potential depth and curvature, reflecting quantum gravity corrections to the nozzle acoustic geometry.

The analysis of effective potential modulation by quantum gravity corrections shows trends across integer spin s and multipole ℓ configurations. As the quantum gravity correction parameter c_6 increases, the peak of the effective potential shifts farther from the analog event horizon at $x = 0$. This trend has strong linear correlations, with the coefficient of determination $R^2 \geq 97.8\%$, between c_6 and the longitudinal coordinate x at which the peak occurs. However, half-integer values of s and ℓ combinations, such as $s = \ell = 1/2$ in Fig. 4g the limit is $c_6 \approx 0.004$. For $s = \ell = 0$, Fig. 4a at $x = 1.416$, yielding a linear fit with coefficient of determination $R^2 = 99.5\%$. Similarly, for the scalar case $s = 0$ and $\ell = 1$ illustrated in Fig. 4b shows a comparable displacement from the longitudinal coordinate $x = 1.18$, (for $c_6 = -0.015$, $r_{\text{peak}} = 3.141$, $V_{\text{max}} = 0.072$) to the value $x = 3.826$ (corresponding to $c_6 = 0.005$, $r_{\text{peak}} = 2.928$, $V_{\text{max}} = 0.075$), within $R^2 = 98.7\%$. For higher multipoles ($\ell = 2$), the peak displacement scales with the spin s. In fact, for the scalar case $s = 0$ in Fig. 4d On the other hand, the longitudinal coordinate $x = 2.969$ regards $r_{\text{peak}} = 2.807$ and $V_{\text{max}} = 0.04$, for $c_6 = 0.005$. This non-monotonic displacement suggests a critical threshold beyond which QN modes may exhibit enhanced/diminished quality factors q_n. Across all cases, the astrophysical distance r_{peak} decreases linearly with the quantum gravity-correction parameter c_6. For instance, $\Delta r_{\text{peak}} = 0.314$ for $s = \ell = 0$, and $\Delta r_{\text{peak}} = 0.259$ for $s = \ell = 2$, as c_6 varies from -0.015 to 0.005. Since the values of the QN modes can be obtained by the behavior of the effective potential in the quantum gravitational corrected near-BH region, then the shape of the effective potential, and by such means the configuration of the de Laval nozzle, far from the BH is less significant for the QN modes. Hence, experimental phenomena such as the reflection of waves from boundaries and surface friction are expected not to influence the observed apparatus.

In all plots in Fig. 4, the peak of the effective potential reaches a maximum nearer to [farther from] the nozzle throat when compared to the Schwarzschild solution, for $c_6 < 0$ [$c_6 > 0$]. There is one singular aspect regarding the corrections of the effective potential due to the parameter c_6 driving quantum gravity corrections. For scalar s-wave perturbations, with $s = \ell = 0$ in Fig. 4a A similar picture is verified for $s = 0, \ell = 1$ in Fig. 4b –4h and $s = 0, \ell = 1$ the asymptotic value of the effective potential starts to differ, for substantially different values of c_6, being the effective potential not negligible whatsoever. For all other values of s and ℓ here analyzed, a similar behavior is observed.

The geometric profile of the de Laval nozzle can now be determined, as its effective potential governing perturbations replicates the one for the quantum-corrected Schwarzschild metric (8). This correspondence enables the derivation of the nozzle critical spatial configuration, as demonstrated numerically in Fig. 5.

The longitudinal profile of the de Laval nozzle, particularly its maximum cross-sectional area A_{MAX} (for instance, at $x = 20$), is very influenced by the multipole number ℓ and spin s. As illustrated in Fig. 5, larger values of ℓ make the nozzle to expand. In fact, for $s = 0$ the cross-sectional area A_{MAX} increases from 6.22 (for $\ell = 0$ in Fig. 5a) to 72.17 (for $\ell = 1$ in Fig. 5b), and to 1101.28 (for $\ell = 2$ in Fig. 5d). On the other hand, the value of spin s reduces the cross-sectional area A_{MAX}, though less prominently. For $\ell = 1$, increasing s from 0 to 1 decreases A_{MAX} by 40%, from 72.17 to 43.28, which is depicted in Figs. 5band 5c –5f

One also concludes from the plots in Figs. 5g and 5hhigher the absolute value of c_6, the more evident the difference between the quantum gravitational corrections to the nozzle geometry and the standard geometry provided by the Schwarzschild solution. In the fermionic perturbation case, positive values of c_6 that widen the nozzle shape with respect to the Schwarzschild solution are derisive, and any effect of quantum-corrections onto the nozzle geometry essentially makes the cross-sectional area shrink proportionally to the absolute value of c_6. The higher the absolute value of c_6, the less steep the nozzle cross-sectional area increases along the longitudinal coordinate. Figures 5a –5f show that bosonic perturbations (scalar, vector, and tensor ones) yield the quantum gravity-corrected nozzle cross-sectional area to decrease [increase] for negative [positive] values of c_6.

In subsonic flows, sound propagates through the gas flowing along the nozzle axis of symmetry, from gas inlet to exhaust gas exit. At the nozzle throat, where the cross-sectional area attains the minimum value, the fluid flow velocity becomes locally sonic, with the Mach number equaling unit, which is a situation that characterizes a choked flow. As the de Laval nozzle cross-sectional area increases, the fluid flow expands and increases to a supersonic velocity, where a sound wave does not propagate backward through the gas, as observed with respect to the reference frame of the nozzle. The Mach number M has a dependence on the longitudinal coordinate x along the de Laval nozzle, as illustrated in Fig. 6. It corroborates to the transition from a subsonic ($M < 1$) to a supersonic ($M > 1$) flow, which numerically occurs precisely *at* the nozzle throat, corresponding to the acoustic horizon. Beyond this point, the diverging nozzle geometry facilitates the fluid flow expansion, driving the Mach number M to supersonic regimes. For fixed values of s and ℓ, the M increment rates increase with larger values of the quantum-correction parameter c_6. It is worth emphasizing that only $s = 1/2$, as discussed before, breaks the linearity near $c_6 \approx 0.002$. The multipole number ℓ amplifies the maximum value of the Mach number M_{MAX}. For $s = 0$,

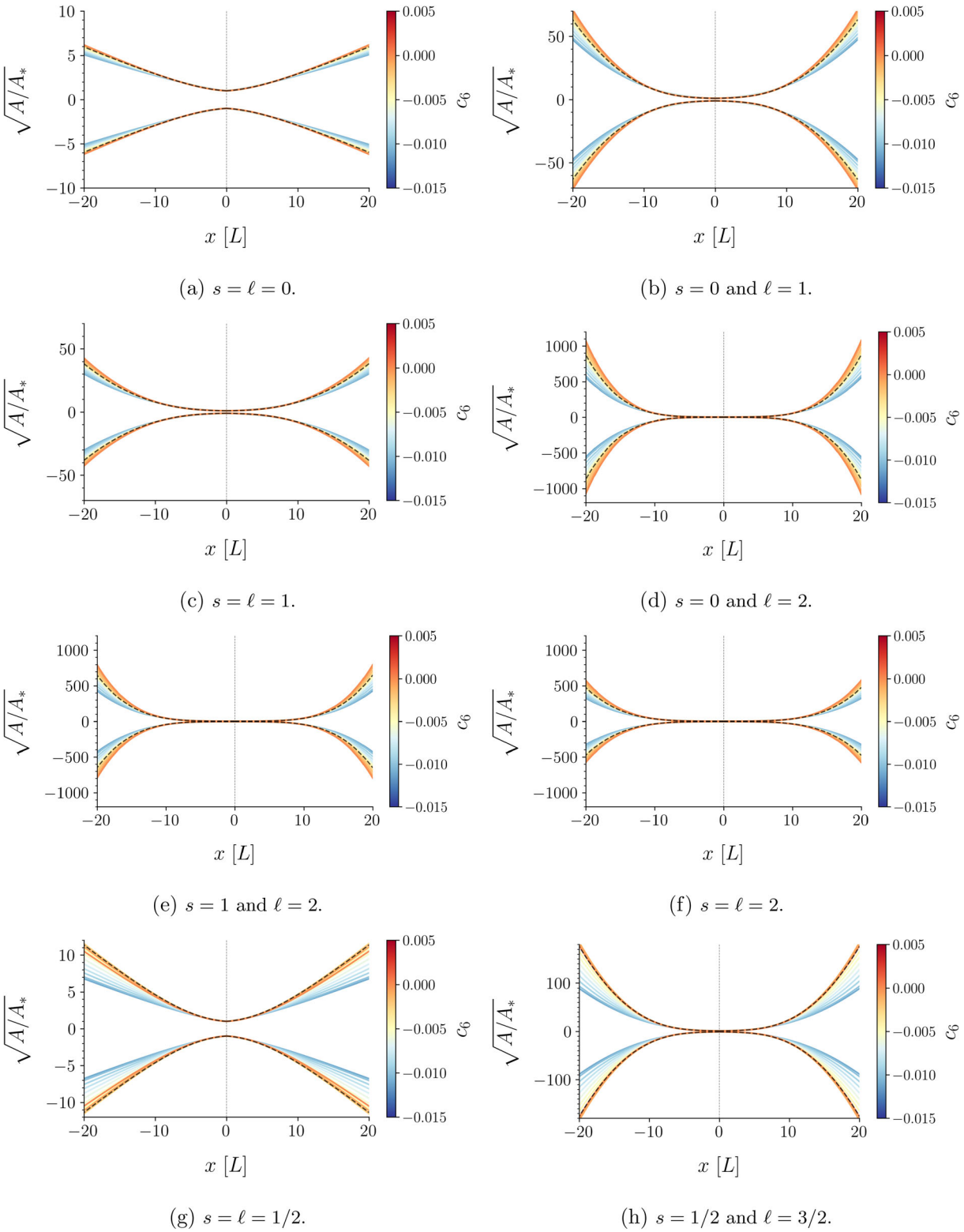

(a) $s = \ell = 0$. (b) $s = 0$ and $\ell = 1$.

(c) $s = \ell = 1$. (d) $s = 0$ and $\ell = 2$.

(e) $s = 1$ and $\ell = 2$. (f) $s = \ell = 2$.

(g) $s = \ell = 1/2$. (h) $s = 1/2$ and $\ell = 3/2$.

Fig. 5 Nozzle shape geometry as a function of the longitudinal direction of the de Laval nozzle, varying c_6 for the quantum-corrected Schwarzschild metric (8). The dashed black line represents the Schwarzschild solution. The values are calculated using $G_N = M = 1$

M_{MAX} increases from 5.56 (for $\ell = 0$ in Fig. 6a) to 16.04 (for $\ell = 1$ in Fig. 6b), and to 48.20 (for $\ell = 2$ in Fig. 6d). On the other hand, the increase in the spin s reduces the Mach number M_{MAX}, although with less efficacy. For $\ell = 1$, increasing s from 0 to 1 makes the Mach number to decrease by $\sim 19\%$, from $16.04 \rightarrow 13.00$, as illustrated in Figs. 6b and 6c

The pressure, temperature, and density profiles of the fluid, measured relative to reservoir quantities, show distinct dependencies on the parameter c_6 within the quantum-corrected BH metric (8). While a visual inspection displays small variations in these profiles across different values of s and ℓ, the comparative analysis presents interesting deviations between extreme values of c_6, with lower bound $c_6 = -0.015$ and upper bound $c_6 = 0.005$. For $s = \ell = 0$, relative variations at the longitudinal coordinate $x = 20$ amount to 61.5% for the pressure, 13.9% for the temperature, and 31.1% for the density. The most pronounced variation occurs for fermionic perturbations, $s = \ell = 1/2$, with relative changes of 73.2% in the pressure, 28.1% in the temperature, and 55.8% in the density, marking the largest observed deviation across the cases here scrutinized. There is a convergence point $x = (6.697 \pm 0.203)$ for scalar fields ($s = 0$), where the quantum-corrected metric (8), independently of the values of c_6, aligns with Schwarzschild solutions. This singular point suggests regimes where quantum gravitational corrections [1] yield observables indistinguishable from classical Schwarzschild BHs. This phenomenon is absent in prior analyses of effective potentials or QN modes. For other combinations of integer values for s and ℓ, maximum variations are on average 40%. All curves converge at $x = 0$ at the nozzle throat, diverging thereafter as c_6 modulates expansion rates. Compared to the Schwarzschild solution, all the curves (p, T, or ρ) either grow or shrink up to a certain point and then reverse direction, remaining until the end of the nozzle. For extreme c_6 values these points include: for $s = \ell = 0$, $x = (3.046 \pm 0.015)$ (for $c_6 = -0.015$) and $x = (4.561 \pm 0.005)$ (for $c_6 = 0.005$). When $s = \ell = 1$, we have $x = (3.571 \pm 0.183)$ (for the lower limit $c_6 = -0.015$) and $x = (5.451 \pm 0.022)$ (for the upper limit $c_6 = 0.005$). In the case where $s = \ell = 2$, we verify that $x = (5.023 \pm 0.082)$ (for $c_6 = -0.015$) and $x = (6.431 \pm 0.054)$ (for $c_6 = 0.005$). Different from what was discussed before, the spin s is more influential than the multipole number ℓ on inflection point positions, as evidenced by mixed configurations. In fact, for $s = 0, \ell = 1$ we have $x = (4.660 \pm 0.035)$ for $c_6 = -0.015$ and $x = (5.198 \pm 0.001)$ when the upper limit $c_6 = 0.005$ is attained. Also, for $s = 1, \ell = 2$ we conclude that $x = (3.839 \pm 0.039)$ for $c_6 = -0.015$ and $x = (5.613 \pm 0.069)$ for $c_6 = 0.005$.

The relative pressure profiles across all configurations in Fig. 7 demonstrate asymptotic decay to zero as $x \gg 1$ and approach unity for $x \rightarrow -\infty$, confirming that a choked flow at the nozzle throat occurs exclusively when both the stagnation pressure and mass flux meet the threshold required to reach sonic velocities. Below this critical threshold, the system reverts to subsonic Venturi tube dynamics and does not achieve supersonic acceleration. Therefore, operational viability necessitates an entry pressure substantially exceeding ambient conditions, with stagnation pressure dominating the ambient backpressure to sustain a choked flow and supersonic expansion.

In addition, Fig. 7g for the fermionic perturbations $s = \ell = 1/2$ is the case that manifests the least quantum gravity effects arising from the c_6 that endows the quantum-corrected metric (8). In all other cases analyzed and depicted in Fig. 7, quantum gravity effects arising from the parameter c_6 are perceptible and provide experimental signatures of the quantum-corrected Schwarzschild metric (8).

The relative pressure, along the longitudinal x-coordinate in a de Laval nozzle, is also relevant to estimate the exhaust velocity at the nozzle exit. Supersonic flow is well known to be attained only through the diverging portion of the nozzle. The chamber temperature, which is located at the nozzle inlet, under isentropic conditions differs little from the stagnation temperature or, for chemical rocket propulsion, from the combustion temperature. Hence, the exit velocity can be expressed as

$$u_E = \sqrt{\frac{RT}{\mu}\frac{2\gamma}{\gamma - 1}} \cdot \sqrt{1 - \left(\frac{p_0}{p}\right)^{\frac{1-\gamma}{\gamma}}}, \tag{53}$$

where μ is the molecular weight of the gas under scrutiny (here we consider $\mu = 28.96$ g/mol for dry air), T is the absolute temperature of the inlet gas, p_0 is the total pressure, and p is the relative local pressure to the nozzle throat pressure. Since the ideal gas constant for any particular gas is inversely proportional to the molecular weight, exhaust velocities strongly depend upon the ratio of the absolute nozzle entrance temperature, which is close to the combustion temperature, divided by the average molecular mass of the exhaust gas. Having the profiles of relative pressure along the x-axis, one can determine the exhaust velocity for the quantum-corrected BH metric (8) by applying Eq. (53).

Now Fig. 8 shows the relative temperature to the throat as a function of the x-axis of the de Laval nozzle, for the quantum-corrected Schwarzschild metric (8). One can realize that again the fermionic perturbations $s = \ell = 1/2$ reveal the most visible alterations driven by the quantum-correction parameter c_6, with respect to the Schwarzschild solution. Increasing the absolute value of c_6 towards negative values increases the exhaust temperature beyond the nozzle throat, whose differences compared to the Schwarzschild solution become sharper at the nozzle exit, as depicted in Fig. 8g

Figure 9 depicts the relative density as a function of the longitudinal x-axis of the nozzle, for the quantum-corrected BH metric (8).

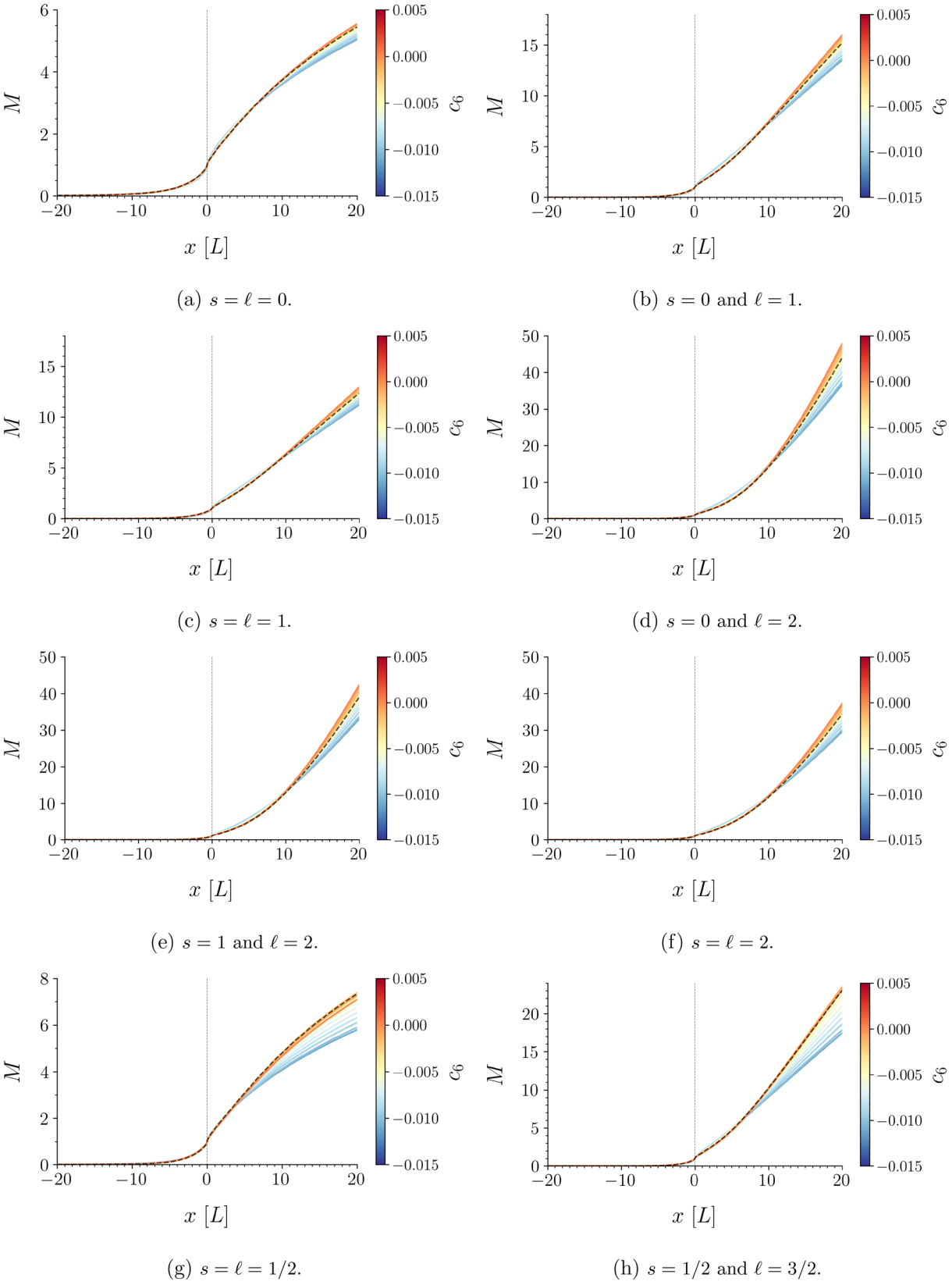

(a) $s = \ell = 0$. (b) $s = 0$ and $\ell = 1$.

(c) $s = \ell = 1$. (d) $s = 0$ and $\ell = 2$.

(e) $s = 1$ and $\ell = 2$. (f) $s = \ell = 2$.

(g) $s = \ell = 1/2$. (h) $s = 1/2$ and $\ell = 3/2$.

Fig. 6 Mach number as a function of the longitudinal direction of the de Laval nozzle, varying c_6 for the quantum-corrected Schwarzschild metric (8). The dashed black line represents the Schwarzschild solution. The values are calculated using $G_N = M = 1$

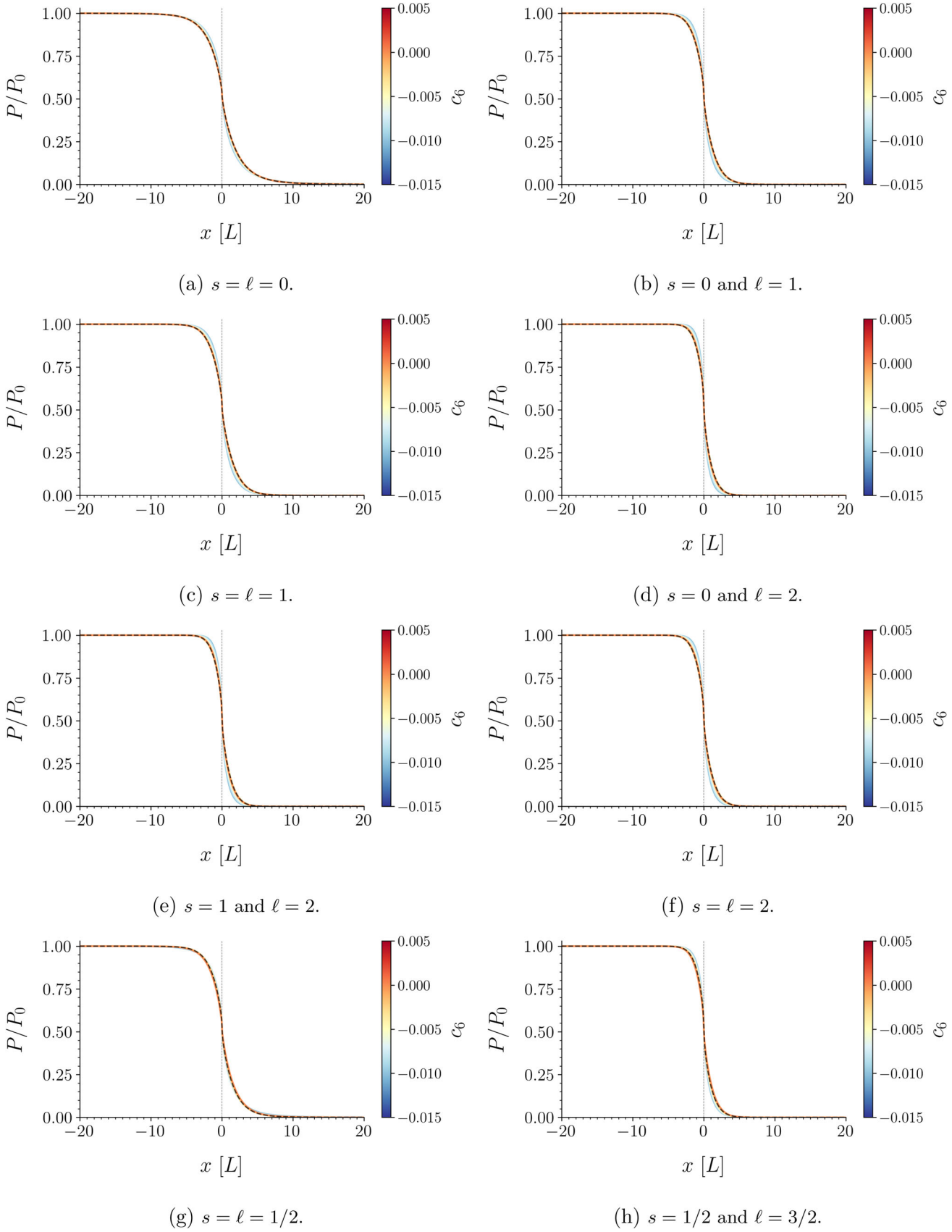

(a) $s = \ell = 0$.

(b) $s = 0$ and $\ell = 1$.

(c) $s = \ell = 1$.

(d) $s = 0$ and $\ell = 2$.

(e) $s = 1$ and $\ell = 2$.

(f) $s = \ell = 2$.

(g) $s = \ell = 1/2$.

(h) $s = 1/2$ and $\ell = 3/2$.

Fig. 7 Relative pressure as a function of the longitudinal direction of the de Laval nozzle, varying c_6 for the quantum-corrected Schwarzschild metric (8). The dashed black line represents the Schwarzschild solution. The values are calculated using $G_N = M = 1$

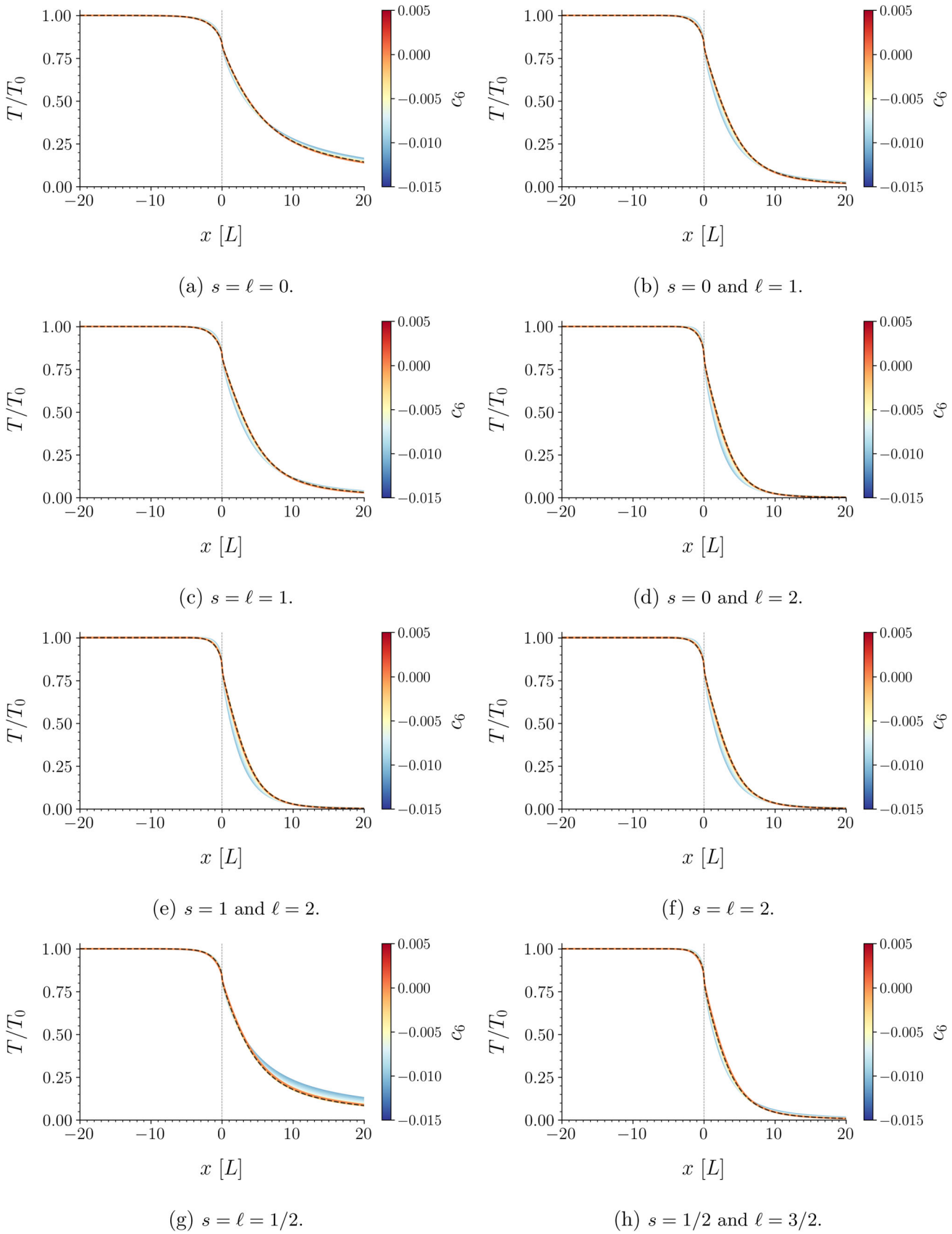

(a) $s = \ell = 0$.

(b) $s = 0$ and $\ell = 1$.

(c) $s = \ell = 1$.

(d) $s = 0$ and $\ell = 2$.

(e) $s = 1$ and $\ell = 2$.

(f) $s = \ell = 2$.

(g) $s = \ell = 1/2$.

(h) $s = 1/2$ and $\ell = 3/2$.

Fig. 8 Relative temperature as a function of the longitudinal direction of the de Laval nozzle, varying c_6 for the quantum-corrected Schwarzschild metric (8). The dashed black line represents the Schwarzschild solution. The values are calculated using $G_N = M = 1$

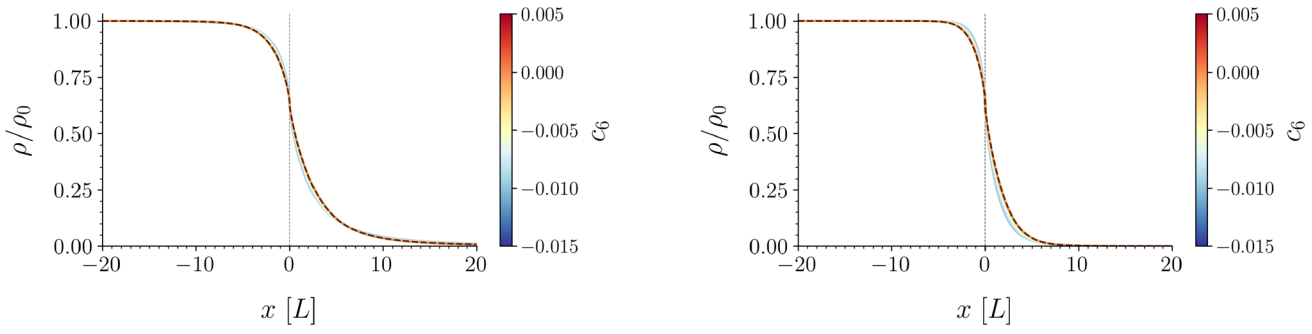

(a) $s = \ell = 0$.

(b) $s = 0$ and $\ell = 1$.

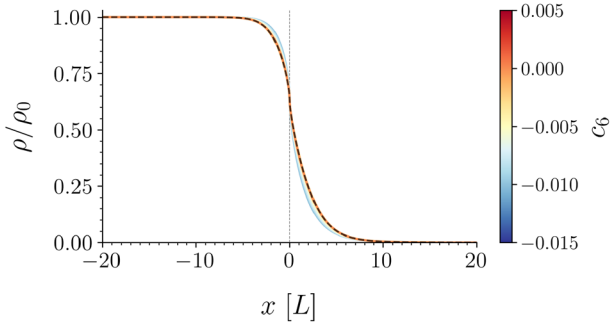

(c) $s = \ell = 1$.

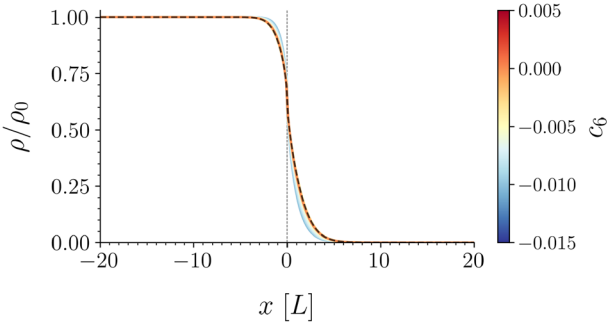

(d) $s = 0$ and $\ell = 2$.

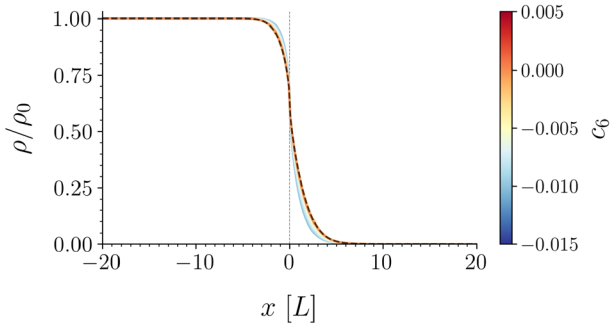

(e) $s = 1$ and $\ell = 2$.

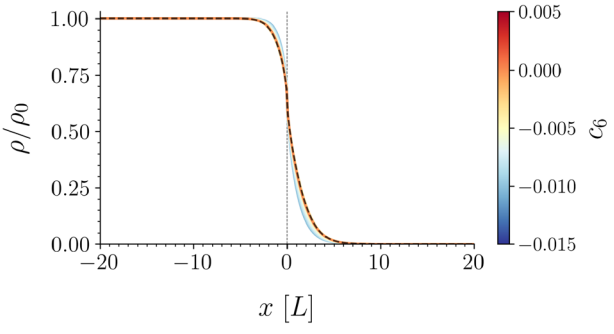

(f) $s = \ell = 2$.

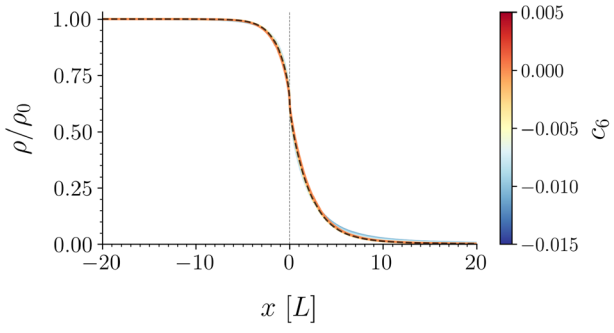

(g) $s = \ell = 1/2$.

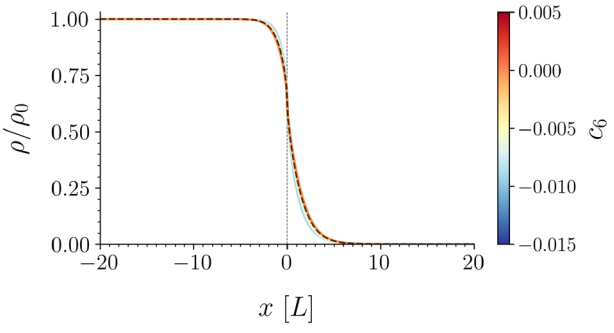

(h) $s = 1/2$ and $\ell = 3/2$.

Fig. 9 Relative density as a function of the longitudinal direction of the de Laval nozzle, varying c_6 for the quantum-corrected Schwarzschild metric (9). The dashed black line represents the Schwarzschild solution. The values are calculated using $G_{\mathrm{N}} = M = 1$

The thermodynamic variables, the nozzle geometry, and the Mach number are the realistic quantities aimed to be measured from a de Laval nozzle in a propulsion laboratory, regarding the quantum-corrected BH metric (8).

The total impulse generated by a nozzle is proportional to the total energy released by or into all the propellants utilized by propulsion systems. The power transmitted by the de Laval nozzle is the product of the thrust generated by the nozzle and the fluid flow velocity. The thrust generated by the nozzle, in a vacuum, can be described as [61]

$$F_{\text{THRUST}} = p_0 \mathrm{A}_\star \left[\sqrt{\frac{2\gamma^2}{\gamma-1}\left(\frac{2}{\gamma+1}\right)^{\frac{\gamma+1}{\gamma-1}}} \left(1 - p^{\frac{\gamma-1}{\gamma}}\right)^{1/2} + \frac{\mathrm{A_E}}{\mathrm{A}_\star}\frac{p_\mathrm{E}}{p_0}\right], \tag{54}$$

where p_E denotes the pressure at which the gas exits the de Laval nozzle, $\mathrm{A_E}$ denotes the area of the nozzle endpoint, and p is the relative local pressure to the throat pressure. Equation (54) shows that the thrust generated by the nozzle is proportional to the throat cross-sectional area, the nozzle inlet pressure, and the pressure ratio across the nozzle. A more detailed numerical analysis indicates that for realistic nozzles at higher external pressures, some flow separation begins to arise within the divergent part of the de Laval nozzle. The cross-sectional area of the exiting supersonic jet will be lower than the cross-sectional area of the nozzle itself, although, to a steady fluid flow the separation typically persists longitudinally. As external pressure rises, the separation point moves upstream. At the nozzle exit, the separated flow continues to be supersonic in the central region however, it is bounded by an annular subsonic flow. Along their interface, there is a discontinuity, yielding the thrust generated by the nozzle to decrease, compared to an ideal de Laval nozzle. These discontinuities may generate shock waves [79].

Another way to quantify the thrust is by the effective exhaust velocity c. With this definition, the thrust generated by the nozzle is simplified to

$$F_{\text{THRUST}} = \dot{m}c, \tag{55}$$

where $\dot{m}$ is mass flux. The effective exhaust velocity is shown in the plots in Fig. 10. Following what was discussed, the thrust is highly dependent on the quantum gravity correction parameter c_6. In all integer s and ℓ cases, the higher the parameter c_6 the higher the thrust at the nozzle endpoint is. By knowing the constant value of mass flux, one can determine the thrust generated by the nozzle and measure it in a real model. In all cases, the effective exhaust velocity increases as a function of the longitudinal nozzle coordinate x.

However, for each fixed value of integer s and ℓ, for any fixed positive [negative] value of the quantum gravity-correction parameter c_6, the exhaust velocity for the quantum-corrected BH metric (8) increases faster [slower] along x than the Schwarzschild solution. Now, for $s = 0$, $\ell = 0$ and for fixed values of c_6, the rate of variation of the effective exhaust velocity with respect to the x coordinate is negative, and the rate decrement steeper is for negative values of c_6, as plotted in Fig. 10a the rate of variation of the effective exhaust velocity with respect to the x coordinate is always positive, irrespectively the value of c_6, and it grows faster for positive values of c_6. A drastically different scenario is verified in Fig. 10g for the case $s = \ell = 1/2$, where almost all the values of c_6 drive the effective exhaust velocity to vary slower as a function of the x coordinate, the higher the value of c_6 is. An analogous result is observed for $s = \ell = 1/2$ in Fig. 10h

The thrust coefficients calculated for all the nozzles are shown in Fig. 11. The efficiency of the nozzle in converting thermal energy into kinetic energy is related to the thrust coefficient, C_F, defined as

$$C_F = \frac{F_{\text{THRUST}}}{p_0 \mathrm{A}_\star}. \tag{56}$$

The thrust coefficient estimates the thrust that is amplified by the expansion of fluid as it flows through the nozzle, compared to the thrust triggered if the compression chamber were connected only to both the convergent section and the nozzle throat, but not to the divergent section. Dividing Eq. (54) by the term $p_0 \mathrm{A}_\star$, one obtains

$$C_F\left(x\right) = \sqrt{\frac{2\gamma^2}{\gamma-1}\left(\frac{2}{\gamma+1}\right)^{\frac{\gamma+1}{\gamma-1}}} \left(1 - p(x)^{\frac{\gamma-1}{\gamma}}\right)^{1/2} + \mathrm{A}(x)p(x). \tag{57}$$

Again, we use the cross-sectional area A and the pressure measured in units of the throat cross-sectional area, $\mathrm{A}_\star$, and total pressure, p_0, respectively. The thrust coefficient in de Laval nozzles represents the efficiency of throwing gases out of the nozzle, measuring the de Laval nozzle's capacity to turn internal pressure into velocity at the nozzle exit. A higher value of the thrust coefficient complies with a more effective performance of the de Laval nozzle.

4.2 QN modes, eigenfrequencies, and overtones of quantum gravitational corrected black holes

After scrutinizing the main features of the quantum gravitational corrected analog de Laval nozzle, the QN mode frequencies can now be computed. A complex QN frequency ω_n defines a QN mode, appearing in the Schrödinger-like eq. (16), on the gravitational side, and in Eq. (31), for its aerodynamic counterpart. Deriving QN modes analytically is often a challenging task, but approximation methods can simplify the process. Among these, the Mashhoon procedure

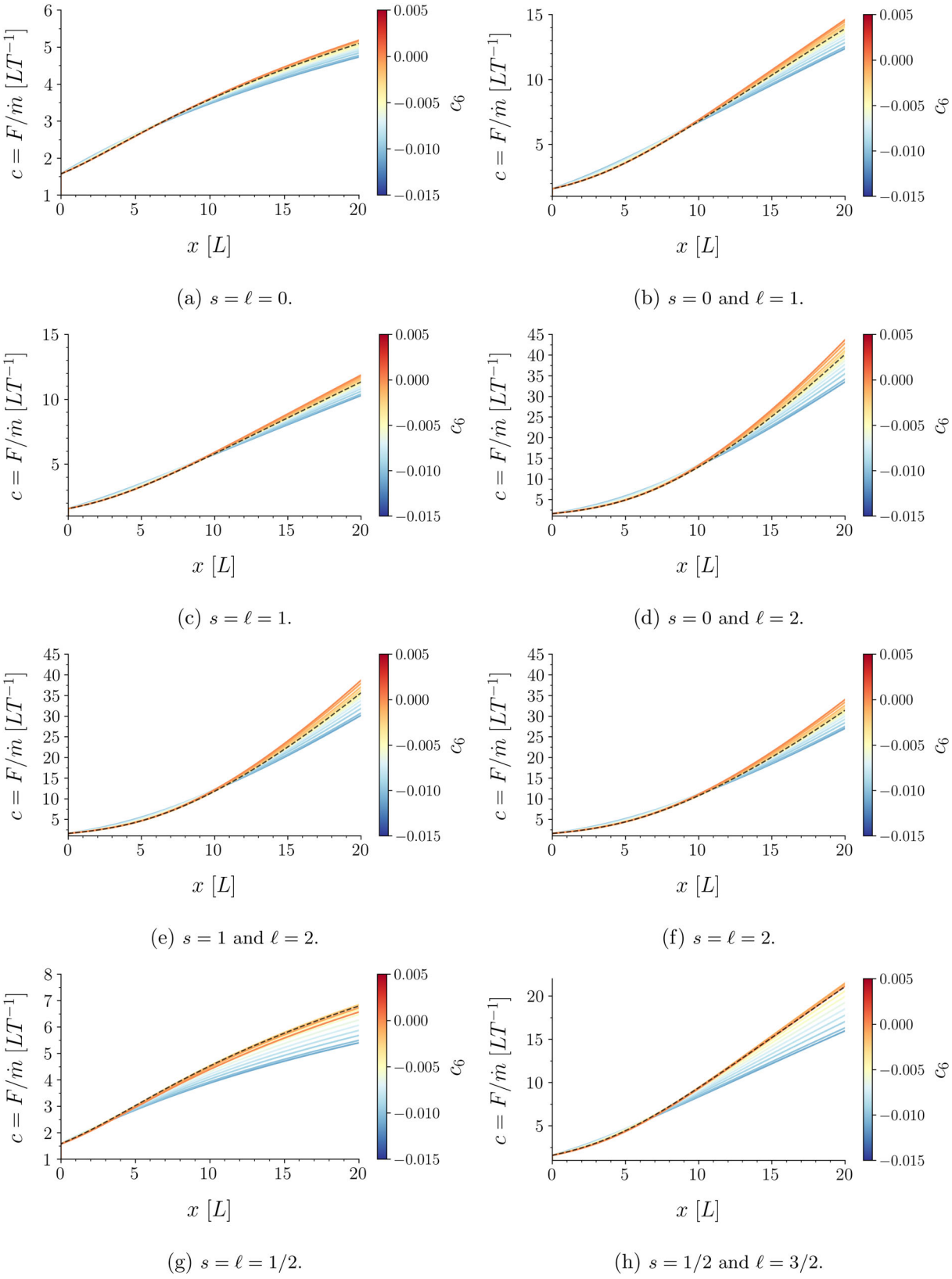

(a) $s = \ell = 0$. (b) $s = 0$ and $\ell = 1$.

(c) $s = \ell = 1$. (d) $s = 0$ and $\ell = 2$.

(e) $s = 1$ and $\ell = 2$. (f) $s = \ell = 2$.

(g) $s = \ell = 1/2$. (h) $s = 1/2$ and $\ell = 3/2$.

Fig. 10 Effective exhaust velocity as a function of the longitudinal direction of the de Laval nozzle, varying c_6 for the quantum-corrected Schwarzschild metric (8). The dashed black line represents the Schwarzschild solution. The values are calculated using $G_{\rm N} = M = 1$

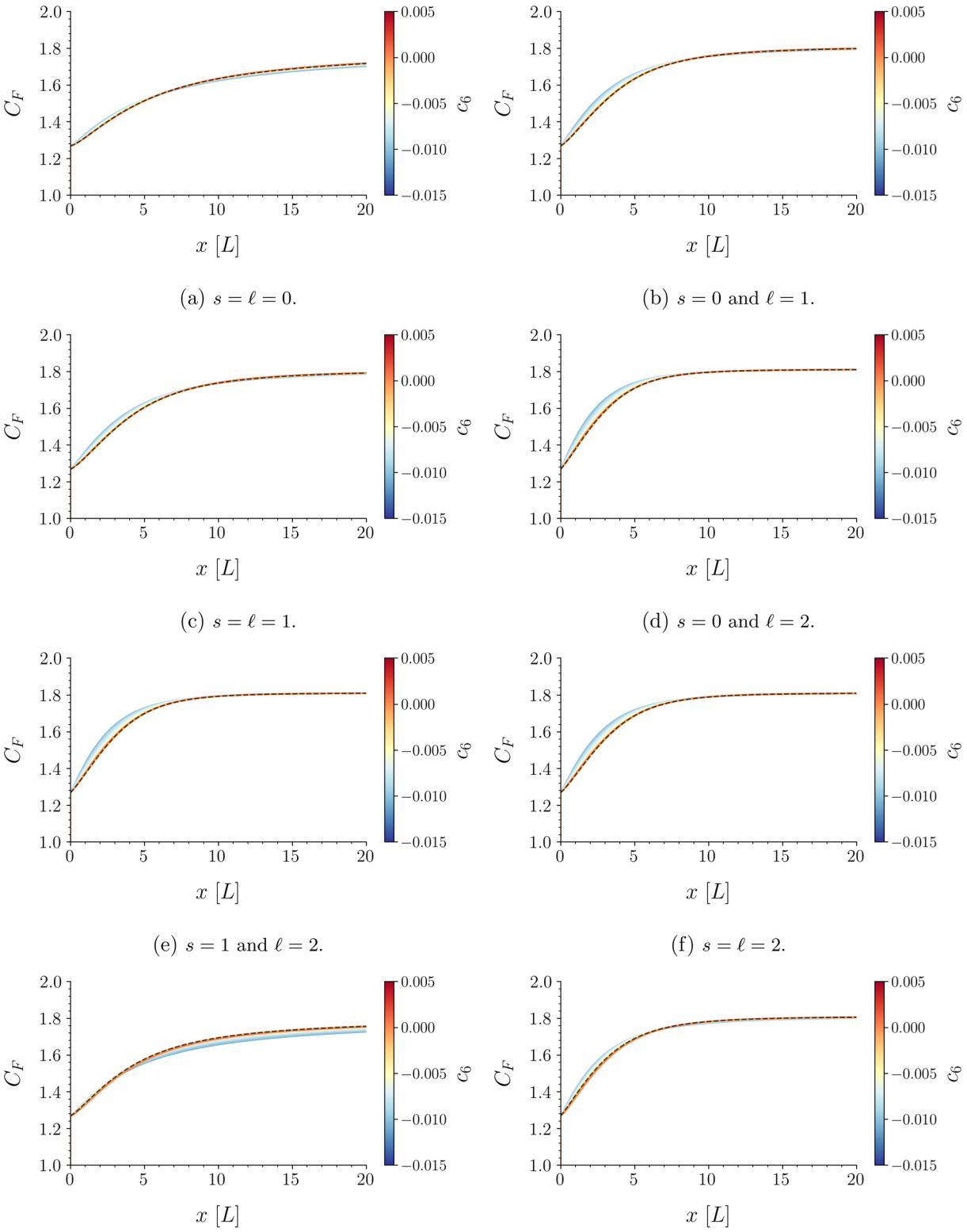

(a) $s = \ell = 0$. (b) $s = 0$ and $\ell = 1$.

(c) $s = \ell = 1$. (d) $s = 0$ and $\ell = 2$.

(e) $s = 1$ and $\ell = 2$. (f) $s = \ell = 2$.

(g) $s = \ell = 1/2$. (h) $s = 1/2$ and $\ell = 3/2$.

Fig. 11 Thrust coefficient as a function of the longitudinal direction of the de Laval nozzle, varying c_6 for the quantum-corrected Schwarzschild metric (8). The dashed black line represents the Schwarzschild solution. The values are calculated using $G_{\rm N} = M = 1$

is employed in this work due to its clarity and practicality [80]. The boundary conditions for QN modes in asymptotically flat BHs, such as the one studied here, are well justified from an astrophysical perspective [42]. The difficulty in calculating QN modes for many BHs typically arises from the slow decay of the effective potential at radial infinity. It introduces a branch cut and causes GWs to scatter off the effective potential, generating backwards tails. The Mashhoon method bypasses these issues by using a Pöschl–Teller effective potential

$$V_{\rm PT}(r_\star) = \frac{V_0}{\cosh^2[\xi(r_\star - r_{\star 0})]}, \tag{58}$$

for $V_0 = V(r_0)$ being the maximum value of the potential,

$$\xi = \sqrt{-\frac{1}{2V_0}\lim_{r\to r_0}\frac{{\rm d}^2 V}{{\rm d}r_\star^2}} \tag{59}$$

is the inverse of the width of the potential, and the constant $-2V_0\xi$, indicates the curvature of the potential at its supremum value. The Pöschl–Teller effective potential (58) decays exponentially in the $r_\star \to \infty$ limit. The boundary conditions for the Schrödinger-like equation demand that the wave function vanish at the boundary. As a result, QN modes correspond to bound states for the new ($V_{\rm PT} \mapsto -V_{\rm PT}$) effective potential. The QN mode frequencies are given by [42,53,80]:

$$\omega_n = \pm\sqrt{V_0 - \frac{\xi^2}{4}} + i\,\xi\left(n + \frac{1}{2}\right), n \in \mathbb{N}. \tag{60}$$

In Eq. (60), $n \in \mathbb{N}$ denotes the overtone number [42,53,81]. Including higher overtones yields a precise description of the GW form well before the fundamental mode dominates. The determination of overtones also extends the regime over which BH perturbation theory is suitable to a time interval even before the GW peak strain amplitude. In addition, the ringdown of the quantum-corrected BH can be analyzed by the inclusion of higher overtones, providing more accurate estimates of the quantum-corrected BH remnant spin and mass [81,82]. The analogy of these overtones is intended to improve the extraction of information from quantum gravity-corrected BH sources from noisy LIGO/Virgo data.

Table 1 presents the QN mode frequencies for the quantum-corrected Schwarzschild metric across different values of s, ℓ, and n, as well as various choices of the quantum gravity-correction parameter c_6. For fixed c_6, increasing ℓ leads to larger values of $\Re(\omega_n)$. On the other hand, for fixed values of c_6 and ℓ, higher values of the spin s result in smaller values of the real part $\Re(\omega_n)$ of the QN frequency, which is consistent with earlier observations. For fixed spin s and multipole moment ℓ, corresponding to fixed $\Re(\omega_n)$ values, higher overtones increase the pure imaginary part of the QN eigenfrequency $\Im(\omega_n)$. Finally, when s, ℓ, and n are fixed integers, increasing $c_6 > 0$ reduces both $\Re(\omega_n)$ and $\Im(\omega_n)$.

As discussed in Ref. [57], the nozzle quality factor $q_n \sim \Re(\omega_n)/\Im(\omega_n)$ is directly related to the number of oscillation cycles during the damping process. The quality factor can be expressed as a function of the maximum value of the Pöschl–Teller effective potential as

$$q_n \sim \frac{\Re(\omega_n)}{\Im(\omega_n)} = \frac{1}{\left(2n+1\right)}\sqrt{\frac{4V_0}{\xi^2} - 1}, \tag{61}$$

and higher overtones result in lower values of q_n. When the quantum gravity correction parameter vanishes, $c_6 = 0$, the Schwarzschild case is recovered, which aligns with previous results in the literature, such as those presented in Ref. [50]. The plots in Fig. 12 display the QN modes for bosonic perturbations with integer spin s, while Figs. 13 show the results for fermionic spin-1/2 perturbations, including higher QN mode overtones up to $n = 3$. The distributions of the QN modes and their overtones in the complex plane illustrate the relationship between the oscillation QN frequency $\Re(\omega)$ and the damping rate $\Im(\omega)$, where the black dots represent the Schwarzschild solution ($c_6 \to 0$) across all bosonic and fermionic perturbation cases here analyzed. The QN mode frequencies for the quantum-corrected Schwarzschild BH (8) clearly show deviations, driven by the quantum correction parameter c_6, from their Schwarzschild counterparts, particularly for higher values of overtones n. Since QN ringing is typically obscured by noise after only a few damping cycles, it becomes essential to design a de Laval nozzle capable of producing QN modes with higher quality factors to ensure effective detection of QN ringing. In this case, higher quality factors are underdamped systems, combining oscillation at a specific frequency with amplitude decay of the signal. Higher quality factors favor the relative amount of damping to decrease and, in this case, the quantum gravity-corrected BH can ring with a purer tone for an extended amount of time, which is better from the experimental point of view. From Figs. 12 and 13, it is possible to examine the QN mode spectrum and identify configurations that are more likely to yield quality factors suitable for experimental setups.

Figure 12 depicts QN modes for integer spins. For scalar perturbations with $s = 0$ in Figs. 12a -12c Electromagnetic perturbations, corresponding to $s = 1$ in Fig. 12d - 12e Gravitational perturbations ($s = 2$, Fig. 12f) QN modes are similar to the $s = 1$ case. The most negative c_6 (≈ -0.05) reduces $\Re(\omega)$ from 0.435 to approximately 0.407, a 6.4% deviation from Schwarzschild. The quality factor of the fundamental mode increases by approximately 2%, from 4.606 to 4.681.

Figure 13 shows the fermionic perturbations ($s = 1/2$, Fig. 13a -13c). This case exhibits moderate sensitivity to

Table 1 QN modes frequencies ω_n for the quantum-corrected Schwarzschild metric (8), for varying value of c_6, s and ℓ, for overtones $n = 0$, 1 and 2. The values are calculated using $G_N = M = 1$

s	l	n	$c_6 = -0.0014$	$c_6 = -0.006$	$c_6 = 0$	$c_6 = 0.003$	$c_6 = 0.005$
0	0	0	0.1006+0.1396i	0.1046+0.1304i	0.1148+0.1148i	0.1221+0.1024i	0.1271+0.0923i
0	0	1	0.1006+0.4189i	0.1046+0.3911i	0.1148+0.3445i	0.1221+0.3073i	0.1271+0.2768i
0	0	2	0.1006+0.6981i	0.1046+0.6518i	0.1148+0.5741i	0.1221+0.5122i	0.1271+0.4613i
$\frac{1}{2}$	$\frac{1}{2}$	0	0.1706+0.1050i	0.1793+0.1156i	0.1890+0.1048i	0.1869+0.1069i	0.1798+0.1148i
$\frac{1}{2}$	$\frac{1}{2}$	1	0.1706+0.3149i	0.1793+0.3467i	0.1890+0.3143i	0.1869+0.3207i	0.1798+0.3444i
$\frac{1}{2}$	$\frac{1}{2}$	2	0.1706+0.5248i	0.1793+0.5778i	0.1890+0.5238i	0.1869+0.5344i	0.1798+0.5740i
0	1	0	0.2975+0.1082i	0.2977+0.1052i	0.2985+0.1006i	0.2993+0.0972i	0.2999+0.0942i
0	1	1	0.2975+0.3245i	0.2977+0.3157i	0.2985+0.3019i	0.2993+0.2915i	0.2999+0.2827i
0	1	2	0.2975+0.5408i	0.2977+0.5261i	0.2985+0.5032i	0.2993+0.4859i	0.2999+0.4712i
1	1	0	0.2497+0.0970i	0.2520+0.0973i	0.2546+0.0962i	0.2564+0.0948i	0.2579+0.0933i
1	1	1	0.2497+0.2910i	0.2520+0.2919i	0.2546+0.2887i	0.2564+0.2844i	0.2579+0.2798i
1	1	2	0.2497+0.4850i	0.2520+0.4866i	0.2546+0.4811i	0.2564+0.4740i	0.2579+0.4663i
$\frac{1}{2}$	$\frac{3}{2}$	0	0.3756+0.1082i	0.3814+0.1032i	0.3855+0.0991i	0.3868+0.0983i	0.3868+0.0992i
$\frac{1}{2}$	$\frac{3}{2}$	1	0.3756+0.3246i	0.3814+0.3097i	0.3855+0.2972i	0.3868+0.2949i	0.3868+0.2976i
$\frac{1}{2}$	$\frac{3}{2}$	2	0.3756+0.5410i	0.3814+0.5162i	0.3855+0.4954i	0.3868+0.4915i	0.3868+0.4959i
0	2	0	0.4827+0.1010i	0.4850+0.1002i	0.4874+0.0979i	0.4889+0.0958i	0.4902+0.0938i
0	2	1	0.4827+0.3031i	0.4850+0.3005i	0.4874+0.2937i	0.4889+0.2874i	0.4902+0.2813i
0	2	2	0.4827+0.5052i	0.4850+0.5009i	0.4874+0.4895i	0.4889+0.4789i	0.4902+0.4688i
1	2	0	0.4537+0.0970i	0.4576+0.0973i	0.4615+0.0962i	0.4639+0.0948i	0.4658+0.0933i
1	2	1	0.4537+0.2910i	0.4576+0.2919i	0.4615+0.2887i	0.4639+0.2844i	0.4658+0.2798i
1	2	2	0.4537+0.4850i	0.4576+0.4866i	0.4615+0.4811i	0.4639+0.4740i	0.4658+0.4663i
2	2	0	0.4236+0.0936i	0.4293+0.0945i	0.4346+0.0944i	0.4379+0.0935i	0.4404+0.0924i
2	2	1	0.4236+0.2807i	0.4293+0.2836i	0.4346+0.2831i	0.4379+0.2806i	0.4404+0.2773i
2	2	2	0.4236+0.4678i	0.4293+0.4727i	0.4346+0.4718i	0.4379+0.4676i	0.4404+0.4622i
$\frac{1}{2}$	$\frac{5}{2}$	0	0.5676+0.1020i	0.5732+0.0998i	0.5779+0.0975i	0.5803+0.0962i	0.5818+0.0956i
$\frac{1}{2}$	$\frac{5}{2}$	1	0.5676+0.3059i	0.5732+0.2994i	0.5779+0.2924i	0.5803+0.2887i	0.5818+0.2868i
$\frac{1}{2}$	$\frac{5}{2}$	2	0.5676+0.5098i	0.5732+0.4991i	0.5779+0.4873i	0.5803+0.4812i	0.5818+0.4780i

variations of c_6 due to the quantum gravity effects. For $\ell = 1/2$, the most negative c_6 (≈ -0.0125) produces a reduction in $\Re(\omega)$ from 0.189 to approximately 0.171, a 9.7% deviation from Schwarzschild. This corresponds to a quality factor reduction of approximately 10% for the fundamental mode, from 1.804 to 1.623. The effect diminishes for ℓ = 3/2 and ℓ = 5/2, with maximum deviations of approximately 3% and 2% respectively, reinforcing the pattern that higher angular momentum modes display reduced sensitivity to quantum corrections. By taking a close look to the shape of $\Im(\omega) \times \Re(\omega)$ as c_6 varies, the non-monotonic shape suggests a maximum value for $\Re(\omega)$ at the threshold $c_6 \approx 0.002$ for $\ell = 1/2$ (Fig. 13d) and $c_6 \approx 0.004$ for $\ell = 3/2$ (Fig. 13e), just as discussed with effective potential. This behaviour does not appear in the analysis of higher multipoles $\ell > 3/2$.

Comparing the types of bosonic and fermionic perturbations on the quantum gravitational corrected BH with $c_6 \in \Big[-0.015, 0.005\Big]$, in order for all effective potentials to be well behaved, one can determine a rank of sensitivity to quantum corrections. Scalar and fermionic perturbations demonstrate the greatest responsiveness to variations of the quantum correction parameter c_6, with a maximum deviation of the quality factor $q_n \sim \Re(\omega)/\Im(\omega)$ about 38% for scalar and 13% for fermionic fields, followed by electromagnetic (4.5%) and gravitational perturbations (4.1%). Additionally, the impact of c_6 in $\Re(\omega)$ or $\Im(\omega)$ is prominently smaller, indicating that quantum corrections to Schwarzschild geometry manifest more in the resonant properties of quantum gravitational-corrected BHs rather than in the individual frequency or damping characteristics. These quantitative deviations suggest that scalar and fermionic channels would provide the most robust observational signatures of quantum gravitational effects in BH perturbations, potentially

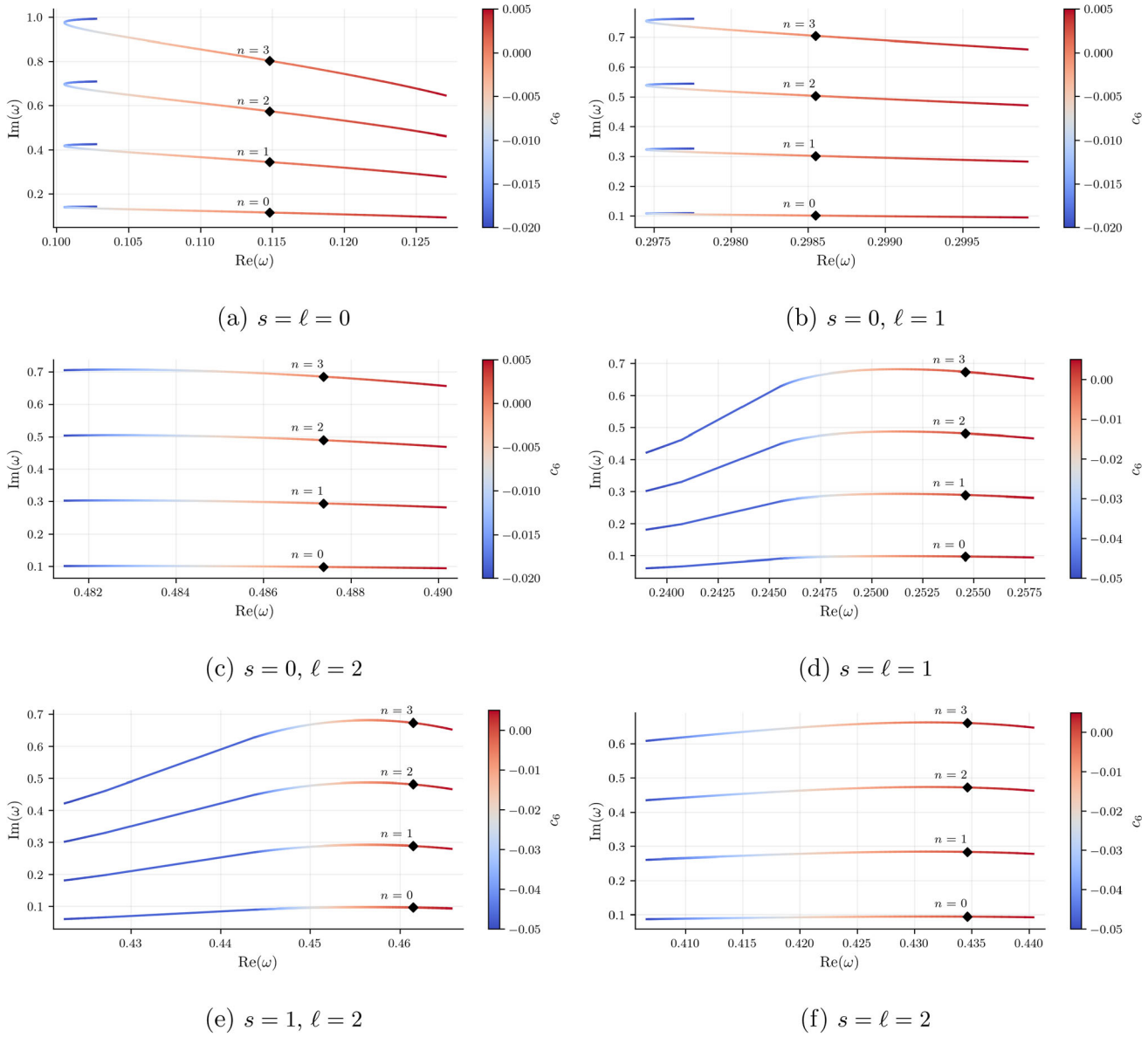

Fig. 12 QN modes frequencies ω_n for spin $s = 0, 1, 2$, with overtones up to $n = 3$, and varying c_6 for the quantum-corrected Schwarzschild metric (8). The black dot represents the Schwarzschild solution. The values are calculated using $G_N = M = 1$

enabling constraints on quantum gravity models through precision measurements of BH ringdown signals.

5 Conclusions

Acoustic BHs that carry quantum gravitational corrections at third order in the curvature can be realized through stable analog transonic fluid flows within a de Laval nozzle, with the quantum-corrected Schwarzschild metric (8) employed to define the analog de Laval nozzle properties in laboratory settings. The QN modes and eigenfrequencies of sound waves in this quantum gravitational-corrected analog BH system were computed, demonstrating their potential to experimentally probe quantum gravitational corrections to BH geometry. Crucially, the wave equations governing scalar and fermionic perturbations in the quantum-corrected BH were shown to map directly onto those describing acoustic perturbations in the de Laval nozzle, with equivalent effective potentials underpinning both systems. We also investigated a vast range of BH masses, from Planck masses to astrophysical ones, showing that quantum gravitational corrections are more evident in primordial BHs. Despite this, astrophysical and stellar BHs were shown to have their analog de Laval nozzle quantities, like the temperature, pressure, exhaust velocity, Mach number, fluid density, and thrust coefficients to be more prominently modified by negative values of the quan-

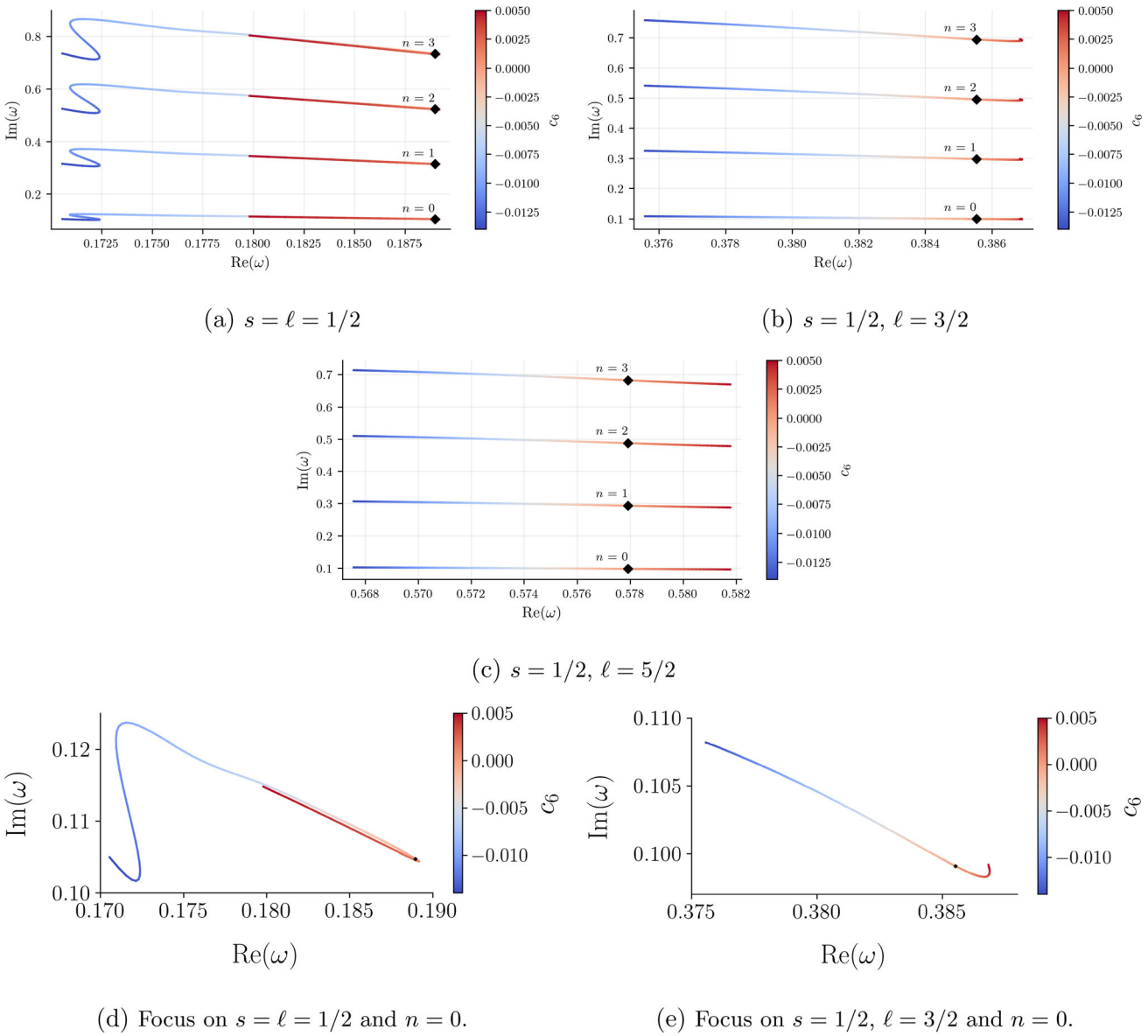

(a) $s = \ell = 1/2$

(b) $s = 1/2$, $\ell = 3/2$

(c) $s = 1/2$, $\ell = 5/2$

(d) Focus on $s = \ell = 1/2$ and $n = 0$.

(e) Focus on $s = 1/2$, $\ell = 3/2$ and $n = 0$.

Fig. 13 QN modes frequencies ω_n for spin $s = 1/2$, with overtones up to $n = 3$, and varying c_6 for the quantum-corrected Schwarzschild metric (8). The black dot represents the Schwarzschild solution. The values are calculated using $G_N = M = 1$

tum gravitational correction parameter c_6, obeying Eq. (52). These quantum gravitational corrections, although somehow tiny, might be macroscopically noticeable in laboratories. Quantum gravitational effects of the nozzle area are almost imperceptible. The quantum gravity parameter c_6 was found to modulate the nozzle geometric profile, the thermodynamic variables, the nozzle geometry, and aerodynamic features, as the Mach number and the thrust coefficient, as well as the QN mode spectrum with special relevance to their overtones. Variations in the parameter c_6 induced shifts in the effective potential peak location (Fig. 4) and altered aerodynamic profiles (Figs. 5–11). Quality factors q_n, derived from QN frequencies, show raised sensitivity to c_6 for spin-0 and spin-1/2 perturbations, with deviations up to 38% and 13%, respectively, compared to electromagnetic and gravitational modes. This emphasizes scalar and fermionic channels as optimal probes for quantum gravity effects in analog experiments. However, spin-2 GW perturbations remain beyond the scope of this hydrodynamic analog. By modelling the ringdown phase of analog acoustic BHs that carry quantum gravitational corrections, with our accurate numerical relativity simulations, we conclude that the fundamental mode alone ($n = 0$) does not suffice to recover all the features of the quantum gravitational-corrected BH. Higher overtones have also been considered, which modify the QN spectrum and carry signatures of quantum gravity effects. It provides

an unbiased estimate of the quantum-corrected BH remnant. The inclusion of higher overtones permits modelling the quantum-corrected BHs ringdown signal for an arbitrary time interval beyond the peak strain GW amplitude. The higher overtones are shown not to be subdominant for quantum-corrected BHs and play a prominent role in modelling the acoustic BH ringdown.

A natural extension of this work involves adding rotation to the quantum-corrected BH model. This would need mapping gravitational perturbations of rotating spacetimes onto quasi-one-dimensional transonic flows, potentially enabling laboratory studies of frame-dragging and ergoregion instabilities. Further investigations could also explore other higher-order curvature corrections, implementing quantum gravity effects to refine the nozzle response to Planck-scale physics.

Funding R.C. is partially supported by the INFN grant FLAG and his work has also been carried out in the framework of activities of the National Group of Mathematical Physics (GNFM, INdAM). C.N.S. thanks CAPES (Grant No. 001). R.d.R thanks the São Paulo Research Foundation – FAPESP (Grants No. 2021/01089-1 and No. 2024/05676-7) and the National Council for Scientific and Technological Development (CNPq) (Grants No. 303390/2019-0 and No. 401567/2023-0).

Data Availability Statement This manuscript has no associated code/software. [Author's comment: The datasets generated during and/or analysed during the current study are available from the corresponding author on reasonable request.]

Code Availability Statement This manuscript has no associated data. [Author's comment: The code/software generated during and/or analysed during the current study is available from the corresponding author on reasonable request.]

Funded by SCOAP[3].

Appendix A: Varying the BH mass: quantum gravitational effects for small values of c_6

For all figures in this Appendix, for the other values of s and ℓ beyond s-wave perturbations studied in this paper, the results are quite identical. Therefore, we will focus on the s-wave perturbations hereon. All plots in this Section show the relative deviation from Schwarzschild, expressed as a percentage:

$$\Delta X = 100\% \times \left(\frac{X_{\rm corrected}}{X_{\rm Schwarzschild}} - 1 \right).$$

Figs. 14a $s = \ell = 0$ and $c_6 = 0.005$ (Fig. 14a)]. The exhaust velocity was evaluated for a representative range of BH masses varying systematically in the range 10^{27} kg $< M < 10^{36}$ kg. Figure 14a considers the differences of the nozzle exhaust velocity, revealing that the decrease of the BH mass makes the exhaust velocity slightly decrease, mainly near the nozzle throat, with maximal decrease around $M \sim 10^{28}$ kg. On the other hand, Fig. 14b regards the negative value $c_6 = -0.01$, illustrating the behaviour of the exhaust velocity. The decrease of the BH mass, until $M \sim M_\odot$ makes the exhaust velocity slightly increase. Although the asymptotic values of the exhaust velocity are practically independent of the BH mass in Fig. 14a depicts a discernible small value ($\ll 1\%$) of the exhaust velocity at the nozzle exit.

Now, the relative temperature to the throat can be analysed as a function of the longitudinal nozzle coordinate x, for values of c_6 obeying Eq. (52). The value $c_6 = 0.005$ was picked in Fig. 15a and $c_6 = -0.01$ is chosen in Fig. 15a , 15b

The relative pressure profiles are depicted in Figs. 16a and 16b as a function of the longitudinal nozzle coordinate x, for distinct stellar and astrophysical masses in the range 10^{27} kg $< M < 10^{36}$ kg, respectively for fixed values of $c_6 = 0.005$ and $c_6 = -0.01$. As shown in Fig. 16a represents the quantum gravitational corrections to the relative pressure profile, which are more manifest for stellar BHs and mainly near the throat (before the horizon), at $|x| \lesssim 0.26\, x_{\rm E}$.

The quantum gravitational corrections of the nozzle cross-sectional area are illustrated in Figs. 17a and 17b as a function of the longitudinal nozzle coordinate x, for astrophysical BH masses in the range 10^{27} kg $< M < 10^{36}$ kg, respectively for fixed values of $c_6 = 0.005$ and $c_6 = -0.01$. From the physical point of view, any quantum gravitational correction in the nozzle area is derisory.

The Mach number is shown in Figs. 18a and 18b as a function of the longitudinal nozzle coordinate x, for distinct astrophysical masses in the range 10^{27} kg $< M < 10^{36}$ kg, respectively for fixed values of $c_6 = 0.005$ and $c_6 = -0.01$. Figure 18a shows that the quantum gravitational corrections are less apparent for $c_6 = 0.005$, when compared to $c_6 = -0.01$ in Fig. 18b and 18b show that the quantum gravitational corrections are more prominent for stellar BH masses. Negative values of c_6 change slightly more the Mach number of stellar BHs when compared to positive values of c_6 (1%-3%).
The relative density profiles are depicted in Figs. 19a and 19b as a function of the longitudinal nozzle coordinate x, for distinct astrophysical masses in the range 10^{27} kg $< M <$

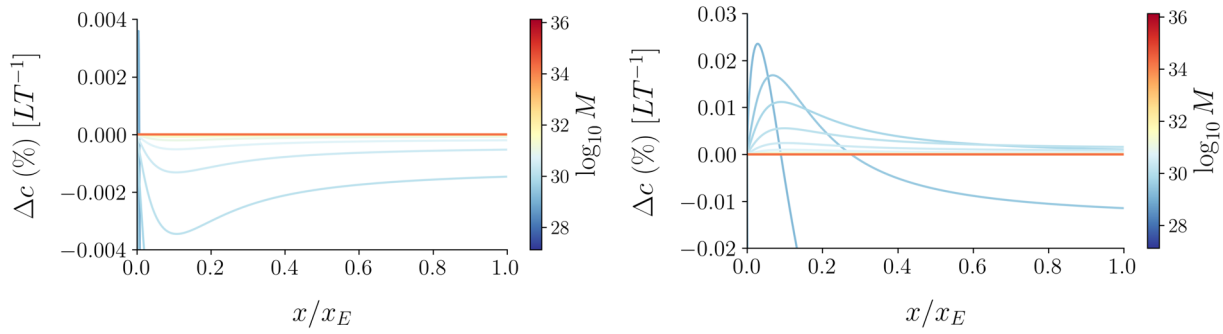

(a) $s = \ell = 0$, $c_6 = 0.005$. (b) $s = 0$ and $\ell = 0$, $c_6 = -0.01$.

Fig. 14 Effective exhaust velocity as a function of the longitudinal nozzle coordinate x, for the quantum-corrected Schwarzschild metric (8), with BH masses in the range 10^{27} kg $< M < 10^{36}$ kg. Relative deviation from Schwarzschild

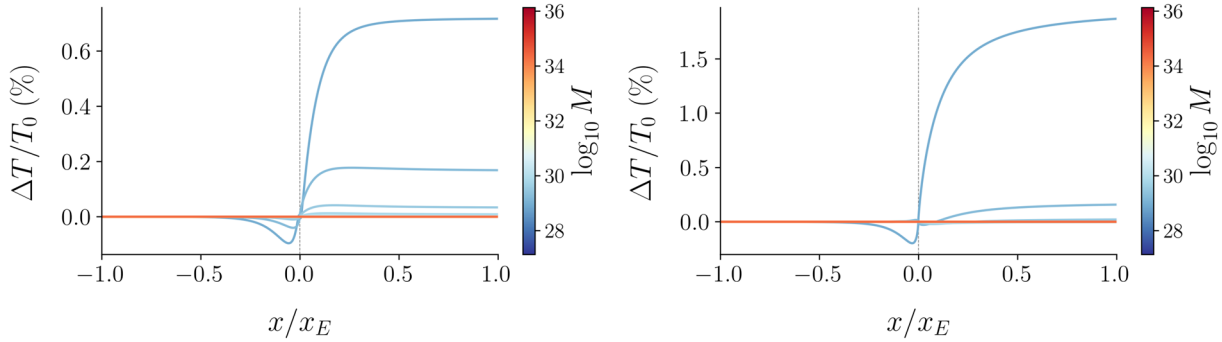

(a) $s = \ell = 0$, $c_6 = 0.005$. (b) $s = 0$ and $\ell = 0$, $c_6 = -0.01$.

Fig. 15 Relative temperature as a function of the longitudinal nozzle coordinate x, for the quantum-corrected Schwarzschild metric (8), with BH masses in the range 10^{27} kg $< M < 10^{36}$ kg.Relative deviation from Schwarzschild

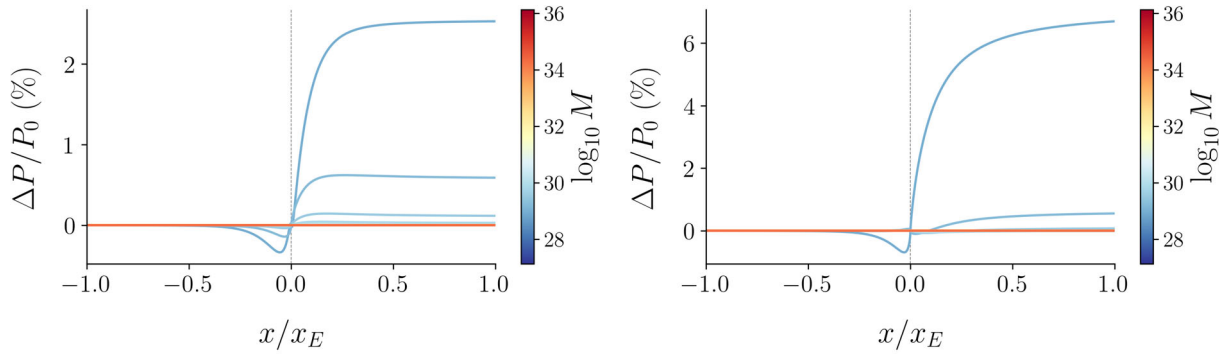

(a) $s = \ell = 0$, $c_6 = 0.005$. (b) $s = 0$ and $\ell = 0$, $c_6 = -0.01$.

Fig. 16 Relative pressure as a function of the longitudinal nozzle coordinate x, for the quantum-corrected Schwarzschild metric (8), with BH masses in the range 10^{27} kg $< M < 10^{36}$ kg.Relative deviation from Schwarzschild

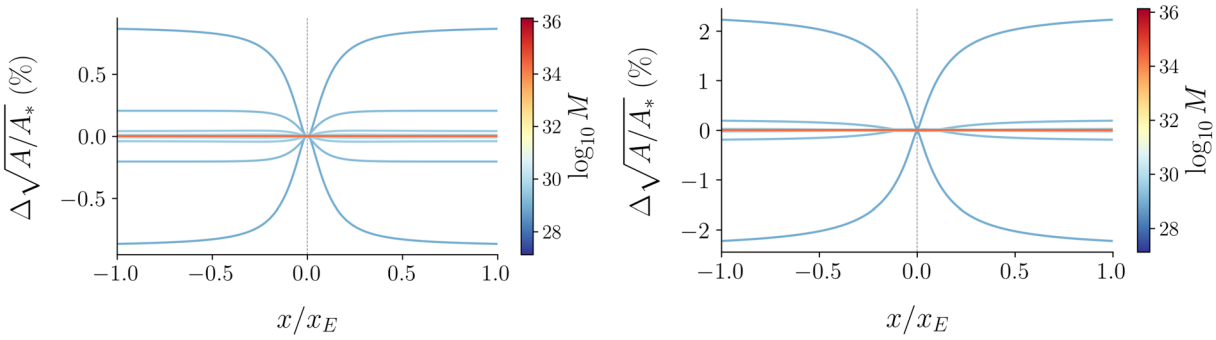

(a) $s = \ell = 0$, $c_6 = 0.005$. (b) $s = 0$ and $\ell = 0$, $c_6 = -0.01$.

Fig. 17 Nozzle shape as a function of the longitudinal nozzle coordinate x, for the quantum-corrected Schwarzschild metric (8), with BH masses in the range 10^{27} kg $< M < 10^{36}$ kg.Relative deviation from Schwarzschild

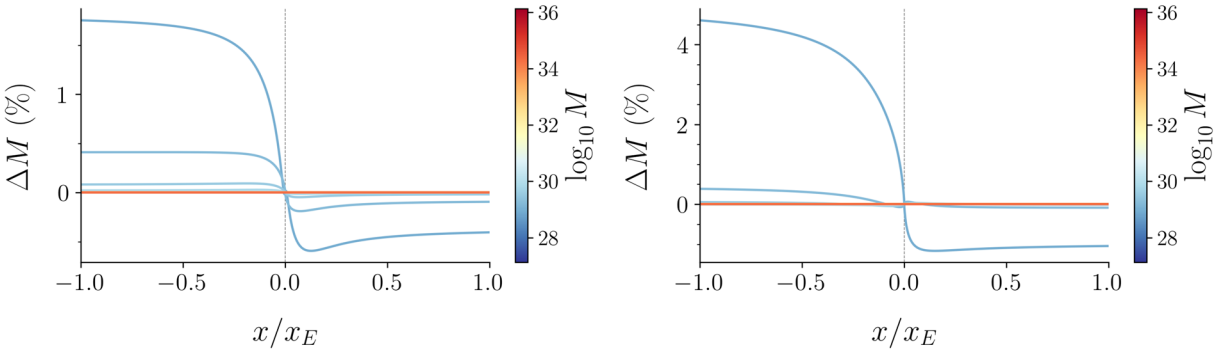

(a) $s = \ell = 0$, $c_6 = 0.005$. (b) $s = 0$ and $\ell = 0$, $c_6 = -0.01$.

Fig. 18 Mach number as a function of the longitudinal nozzle coordinate x, for the quantum-corrected Schwarzschild metric (8), with BH masses in the range 10^{27} kg $< M < 10^{36}$ kg.Relative deviation from Schwarzschild

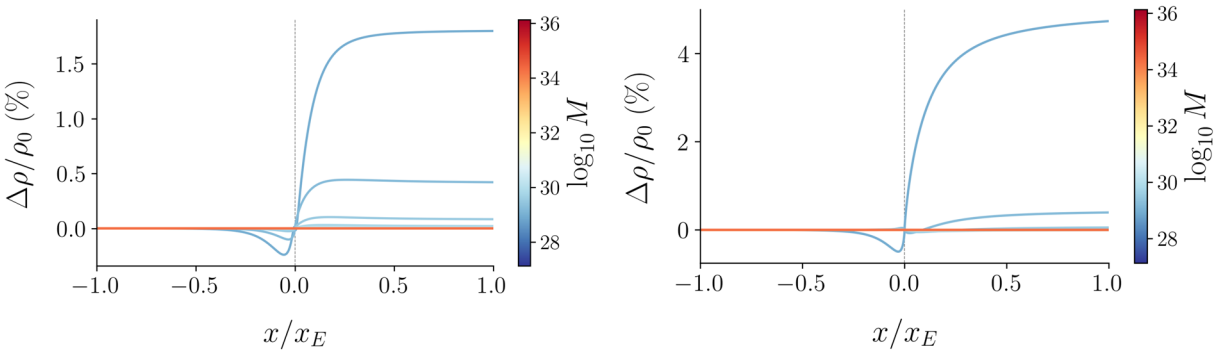

(a) $s = \ell = 0$, $c_6 = 0.005$. (b) $s = 0$ and $\ell = 0$, $c_6 = -0.01$.

Fig. 19 Relative density as a function of the longitudinal nozzle coordinate x, for the quantum-corrected Schwarzschild metric (8), with BH masses in the range 10^{27} kg $< M < 10^{36}$ kg.Relative deviation from Schwarzschild

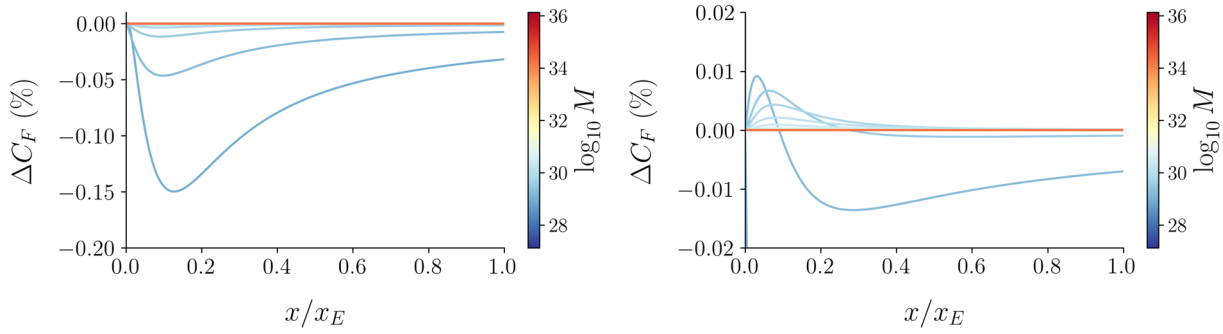

(a) $s = \ell = 0$, $c_6 = 0.005$. (b) $s = 0$ and $\ell = 0$, $c_6 = -0.01$.

Fig. 20 Thrust coefficient as a function of the longitudinal nozzle coordinate x, for for the quantum-corrected Schwarzschild metric (8), with BH masses in the range 10^{27} kg $< M < 10^{36}$ kg.Relative deviation from Schwarzschild

10^{36} kg, respectively for fixed values of $c_6 = 0.005$ and $c_6 = -0.01$. As depicted in Fig. 19a represents the quantum gravitational corrections to the relative pressure profile, which are more manifest for stellar BHs and mainly near the throat (before the horizon), at $|x| \lesssim 0.29\, x_{\rm E}$.

Finally, the thrust coefficient is studied in Figs. 20a and 20b as a function of the longitudinal nozzle coordinate x, for distinct astrophysical masses in the range 10^{27} kg $< M <$ 10^{36} kg, respectively for fixed values of $c_6 = 0.005$ and $c_6 = -0.01$.

Figure 20a shows a less steep increase of the thrust coefficient as a function of the longitudinal nozzle coordinate, for stellar BH masses, when compared to astrophysical BHs. The opposite scenario is observed in Fig. 20b.

References

1. X. Calmet, J. Kuipers, Eur. Phys. J. C **81**, 1146 (2021). arXiv:2105.07325
2. Calmet, X., Casadio, R., Kuipers, F., Phys. Rev. D**100** 086010 (2019). arXiv:1909.13277
3. R. Casadio, A. Kamenshchik, I. Kuntz, Nucl. Phys. B **971**, 115496 (2021). arXiv:2102.10688
4. I. Kuntz, R. Casadio, Phys. Lett. B **802**, 135219 (2020). arXiv:1911.05037
5. M. Asorey, G. Krein, M. Pardina, I.L. Shapiro, JHEP **01**, 113 (2025). arXiv:2408.16514
6. L. Bonora, K.P.S. de Brito, R. da Rocha, JHEP **02**, 069 (2015). arXiv:1411.1590
7. A.O. Barvinsky, Y.V. Gusev, G.A. Vilkovisky, V.V. Zhytnikov, J. Math. Phys. **35**, 3525–3542 (1994). arXiv:gr-qc/9404061
8. S.D. Odintsov, I.L. Shapiro, Class. Quant. Grav. **9**, 873–882 (1992)
9. Z.L. Wang, E. Battista, Eur. Phys. J. C **85**, 304 (2025). arXiv:2501.14516
10. H. Nastase, JHEP **04**, 149 (2016). arXiv:1602.03708
11. I. Perrucci, F. Kuipers, R. Casadio, JCAP **03**, 005 (2025). arXiv:2412.04886
12. X. Calmet, R. Casadio, M. Sebastianutti, Phys. Lett. B **860**, 139208 (2025). arXiv:2408.08229
13. J.F. Donoghue, G. Menezes, Phys. Rev. D **97**, 126005 (2018). arXiv:1804.04980
14. I. Kuntz, R. da Rocha, Nucl. Phys. B **961**, 115265 (2020). arXiv:1909.10121
15. R. Casadio, A. Giugno, A. Giusti, M. Lenzi, Phys. Rev. D **96**, 044010 (2017). arXiv:1702.05918
16. Q. Wang, N. Oshita, N. Afshordi, Phys. Rev. D **101**, 024031 (2020). arXiv:1905.00446
17. G.P. de Brito, A.D. Pereira, A.F. Vieira, Phys. Rev. D **103**, 104023 (2021). arXiv:2012.08904
18. R. Casadio, P. Nicolini, R. da Rocha, Class. Quant. Grav. **35**, 185001 (2018). arXiv:1709.09704
19. D.C. Moreira, R. da Rocha, Class. Quant. Grav. **41**, 235009 (2024). arXiv:2405.01505
20. L.A. Lessa, J.E.G. Silva, Eur. Phys. J. C **84**, 194 (2024). arXiv:2309.07269
21. J. Ovalle, R. Casadio, R. da Rocha, A. Sotomayor, Z. Stuchlik, EPL **124**, 20004 (2018). arXiv:1811.08559
22. D. Bazeia, L. Losano, G.J. Olmo, D. Rubiera-Garcia, Phys. Rev. D **90**, 044011 (2014). arXiv:1405.0208
23. P. Meert, R. da Rocha, Nucl. Phys. B **967**, 115420 (2021). arXiv:2006.02564
24. R. da Rocha, A.A. Tomaz, Eur. Phys. J. C **80**, 857 (2020). arXiv:2005.02980
25. R. da Rocha, Phys. Rev. D **105**, 026014 (2022). arXiv:2111.01244
26. R. da Rocha, J.M. Hoff da Silva, Int. J. Geom. Meth. Mod. Phys. **6**, 461 (2009). arXiv:0901.0883
27. 't Hooft, G., Veltman, M.J.G. Ann. Inst. H. Poincare Phys. Theory A **20**, 69–94 (1974)
28. M.H. Goroff, A. Sagnotti, Nucl. Phys. B **266**, 709–736 (1986)
29. L.A. Lessa, R.V. Maluf, J.E.G. Silva, C.A.S. Almeida, JCAP **05**, 123 (2024). arXiv:2312.06588
30. P. Bueno, P.A. Cano, Phys. Rev. D **94**, 124051 (2016). arXiv:1610.08019
31. A. De Felice, S. Tsujikawa, Phys. Lett. B **843**, 138047 (2023). arXiv:2305.07217
32. L. Rachwal, L. Modesto, A. Pinzul, I.L. Shapiro, Phys. Rev. D **104**, 085018 (2021). arXiv:2104.13980
33. G. Lambiase, R.C. Pantig, A. Övgün, Phys. Dark Univ. **46**, 101597 (2024). arXiv:2406.18292
34. X. Calmet, S.D.H. Hsu, M. Sebastianutti, Phys. Lett. B **841**, 137820 (2023). arXiv:2303.00310
35. J. Matyjasek, Phys. Rev. D **102**, 124046 (2020). arXiv:2009.10793
36. M. Marciu, D.M. Ioan, M. Dragomir, Eur. Phys. J. C **84**, 196 (2024). arXiv:2311.11297
37. A. Bukhari, G. Abbas, H. Rehman, A. Ashraf, E.E. Mahmoud, A.H. Hakami, Eur. Phys. J. Plus **140**, 210 (2025)
38. R. da Rocha, Eur. Phys. J. Plus **139**, 1006 (2024). arXiv:2409.17325

39. K.D. Kokkotas, B.G. Schmidt, Living Rev. Rel. **2**, 2 (1999). arXiv:gr-qc/9909058
40. H.P. Nollert, Class. Quant. Grav. **16**, R159–R216 (1999)
41. V. Cardoso, P. Pani, Living Rev. Rel. **22**, 4 (2019). arXiv:1904.05363
42. R.A. Konoplya, A. Zhidenko, Rev. Mod. Phys. **83**, 793–836 (2011). arXiv:1102.4014
43. B.P. Abbott, (LIGO Scientific, Virgo), et al., Phys. Rev. Lett. **116**, 061102 (2016). arXiv:1602.03837
44. F. Acernese, (VIRGO), et al., Class. Quant. Grav. **32**, 024001 (2015). arXiv:1408.3978
45. J. Cavalcante, a P, Richartz M and da Cunha B C, Phys. Rev. D **110**, 124064 (2024). arXiv:2408.13964
46. V. Cardoso, E. Franzin, P. Pani, Phys. Rev. Lett.**116**, 171101 (2016). [Erratum: Phys.Rev.Lett. 117, 089902 (2016)] . arXiv:1602.07309
47. E. Maggio, A. Testa, S. Bhagwat, P. Pani, Phys. Rev. D **100**, 064056 (2019). arXiv:1907.03091
48. Konoplya R A and Zhidenko A 2022. arXiv:2203.16635
49. J. Abedi, H. Dykaar, N. Afshordi, Phys. Rev. D **96**, 082004 (2017). arXiv:1612.00266
50. R.T. Cavalcanti, R.C. de Paiva, R. da Rocha, Eur. Phys. J. Plus **137**, 1185 (2022). arXiv:2203.08740
51. I. Kuntz, R. da Rocha, Eur. Phys. J. C **79**, 447 (2019). arXiv:1903.10642
52. V. Ferrari, L. Gualtieri, Gen. Rel. Grav. **40**, 945–970 (2008). arXiv:0709.0657
53. E. Berti, V. Cardoso, A.O. Starinets, Class. Quant. Grav. **26**, 163001 (2009). arXiv:0905.2975
54. H. Gong, S. Li, D. Zhang, G. Fu, J.P. Wu, Phys. Rev. D **110**, 044040 (2024). arXiv:2312.17639
55. R. Oliveira, D.M. Dantas, V. Santos, C.A.S. Almeida, Class. Quant. Grav. **36**, 105013 (2019). arXiv:1812.01798
56. M. Visser, Class. Quant. Grav. **15**, 1767 (1998). arXiv:gr-qc/9712010
57. S. Okuzumi, M. Sakagami, a. Phys. Rev. D **76**, 084027 (2007). arXiv:gr-qc/0703070
58. H. Furuhashi, Y. Nambu, H. Saida, Class. Quant. Grav. **23**, 5417–5438 (2006). arXiv:gr-qc/0601066
59. E. Abdalla, R.A. Konoplya, A. Zhidenko, Class. Quant. Grav. **24**, 5901–5910 (2007). arXiv:0706.2489
60. S. Sarkar, A. Bhattacharyay, Phys. Rev. D **96**, 064027 (2017). arXiv:1703.08027
61. R. Casadio, C.N. Souza, R. da Rocha, Eur. Phys. J. C **84**, 767 (2024). arXiv:2402.04682
62. M.A. Anacleto, F.A. Brito, C.V. Garcia, G.C. Luna, E. Passos, Phys. Rev. D **100**, 105005 (2019). arXiv:1904.04229
63. Yang J, Afshordi N, Torabian M, Jafari S A and Baskaran G (2024). arXiv:2412.08517
64. A. Barvinsky, G. Vilkovisky, Nucl. Phys. B **333**, 471–511 (1990)
65. J.F. Donoghue, Phys. Rev. D **50**, 3874–3888 (1994). arXiv:gr-qc/9405057
66. A. Delhom, T. Mariz, J.R. Nascimento, G.J. Olmo, A.Y. Petrov, P.J. Porfírio, JCAP **07**, 018 (2022). arXiv:2202.11613
67. X. Calmet, B.K. El-Menoufi, Eur. Phys. J. C **77**, 243 (2017). arXiv:1704.00261
68. X. Calmet, J. Kuipers, Phys. Rev. D **97**, 086002 (2018). arXiv:1801.07636
69. R.P. Woodard, Scholarpedia **10**, 32243 (2015). arXiv:1506.02210
70. J.Z. Simon, Phys. Rev. D **41**, 3720–3733 (1990)
71. C.P. Burgess, Living Rev. Relativity **7**, 5 (2004). arXiv:gr-qc/0311082
72. J.F. Donoghue, AIP Conf. Proc. **1743**, 020011 (2016). arXiv:1702.00319
73. A. Barvinsky, G. Vilkovisky, Phys. Rept. **119**, 1–74 (1985)
74. B. Holdom, J. Ren, Phys. Rev. D **106**, 025009 (2022). arXiv:2203.00753
75. S.N. Solodukhin, Phys. Lett. B **802**, 135235 (2020). arXiv:1907.07916
76. Dubinsky A (2024). arXiv:2405.13552
77. J. Li, M. Hong, K. Lin, Phys. Rev. D **88**, 064001 (2013). arXiv:1308.6499
78. K.H.C. Castello-Branco, R.A. Konoplya, A. Zhidenko, Phys. Rev. D **71**, 047502 (2005). arXiv:hep-th/0411055
79. L. D. Landau, E. M. Lifshitz, L. D. Landau (1987) *Fluid mechanics* v. 6 (Oxford)
80. V. Ferrari, B. Mashhoon, Phys. Rev. D **30**, 295 (1984)
81. M. Giesler, M. Isi, M.A. Scheel, S. Teukolsky, Phys. Rev. X **9**, 041060 (2019). arXiv:1903.08284
82. A. Buonanno, G.B. Cook, F. Pretorius, Phys. Rev. D **75**, 124018 (2007). arXiv:gr-qc/0610122